THE TRANSLUCENT MOLECULAR CLOUDS TOWARD HD 154368.
I. EXTINCTION, ABUNDANCES, AND DEPLETIONS

THEODORE P. SNOW[1,2,3]
Center for Astrophysics and Space Astronomy, University of Colorado

JOHN H. BLACK[1,2]
Steward Observatory, University of Arizona

EWINE F. VAN DISHOECK[1,2]
Sterrewacht Leiden, Leiden University

GEOFFREY BURKS
Center for Astrophysics and Space Astronomy, University of Colorado

RICHARD M. CRUTCHER[1,2]
Department of Astronomy, University of Illinois

BARRY L. LUTZ[1,2]
Department of Physics and Astronomy, Northern Arizona University

AND

MARGARET M. HANSON AND RALPH Y. SHUPING
Center for Astrophysics and Space Astronomy, University of Colorado
Received 1995 August 15; accepted 1996 January 17

ABSTRACT

We report the results of a comprehensive analysis of a line of sight observed using the Goddard High Resolution Spectrograph (GHRS) on the *Hubble Space Telescope* (*HST*), toward HD 154368, an O9.5 Iab star located about 800 pc away. The line of sight intersects translucent interstellar cloud material, having a color excess $E(B-V) = 0.82$ and known high molecular abundances from ground-based data. The *HST* observations consist of high-resolution spectra obtained with grating ECH-B at wavelengths longward of 1800 Å, and moderate-resolution spectra from grating G160M at shorter wavelengths. We observed some 19 wavelength settings, covering the positions of numerous atomic and molecular transitions. We also incorporate *IUE* and ground-based data in the study, the latter coming from several observatories at visible and millimeter wavelengths.

In this paper we report on the general goals and results of the study, with emphasis on the atomic abundances and depletions. We find that the column densities of most species are slightly higher, relative to the adopted total gas column density, than in some thinner clouds in which most of the absorption arises in a single dense component. Consequently the depletions of elements from the gas phase onto the dust are less than in "typical" diffuse clouds such as the one toward ζ Oph. Most of the gas toward HD 154368 resides in two main clouds, centered near -3.26 and -20.95 km s^{-1} (heliocentric). Our profile analyses show that the depletions in these two clouds are similar. We discuss the possible relationship of this result to the ultraviolet extinction curve toward HD 154368, derived from *IUE* spectra.

Subject headings: dust, extinction — ISM: abundances — ISM: clouds — ISM: molecules — stars: individual (HD 154368) — ultraviolet: ISM

1. INTRODUCTION

The study of *translucent* clouds (i.e., diffuse clouds having total extinctions A_V in the range 2–5 mag) can reveal physical and chemical processes that are intermediate between those occurring in classical diffuse clouds and dark clouds (Crutcher 1985; Black 1985; van Dishoeck & Black 1988a). Translucent clouds are characterized by larger molecular column densities than are normally seen in diffuse clouds, as the chemistry becomes less dominated by photoprocesses than in diffuse clouds. It is in this important regime of cloud thickness that carbon makes a transition from atomic (C$^+$ and C) to molecular form (primarily CO; van Dishoeck & Black 1988b). It is also expected that in translucent clouds gas-grain interactions may have proceeded to an advanced degree, modifying grains through the growth of mantles and enhancing depletions from the gas phase in the process. Translucent clouds are readily observed at visible wavelengths for many lines of sight and have sufficient column densities of several molecular species for millimeter-wave observations to be feasible. Owing to the steep rise of the extinction curve toward short wavelengths, these clouds are difficult to observe by means of high-resolution UV absorption-line techniques. The high UV throughput of the Goddard High Resolution Spectrograph (GHRS) aboard the *Hubble Space Telescope* (*HST*) now makes the observation of translucent clouds feasible.

This paper provides a comprehensive analysis of a particular translucent sight line—that toward HD 154368—which has been observed at many different wavelengths, using several different instruments. This line of sight was chosen because it is known to contain large molecular

column densities from ground-based observations (Blades 1978; Blades & Bennewith 1973; van Dishoeck & de Zeeuw 1984; van Dishoeck & Black 1989; Gredel, van Dishoeck, & Black 1993). The reddening of the star is $E(B-V) = 0.82$, based on the spectral type from Garrison, Hiltner, & Schild (1977), photometry from Schild, Garrison, & Hiltner (1983), and the intrinsic $B-V$ color of -0.30 (e.g., Johnson 1966). This value of color excess is significantly larger than that of any star studied with the *Copernicus* satellite, but the star is still bright enough at ultraviolet wavelengths to perform the *HST* observations. Here we combine visible and near-IR absorption-line measurements obtained at several different telescopes, millimeter-wave data, low- and high-dispersion ultraviolet spectra obtained with the *IUE*, and high-resolution spectra obtained with the GHRS on the *HST*, in order to develop a complete picture of the chemical and physical processes occurring in the cloud. This paper focuses on the atomic data, providing information on column densities and depletions; a second paper (Black et al. 1996, hereafter Paper II) will provide the results of the molecular analysis. The results reported in these two papers represent the first in a series of observations planned with the *HST*, in which we will explore the relationships between gas-phase processes and the properties of the dust, for a variety of environments.

The paper is arranged as follows: the next section contains a detailed summary of the characteristics of the observed line of sight and the relationship of the cloud to the star; § 3 describes the observations made for this study at all the different telescopes employed; § 4 presents the UV extinction curve; § 5 describes the velocity structure in the line of sight, as determined from ultra–high-resolution optical spectra; § 6 presents the atomic column densities for hydrogen and other species; § 7 discusses the depletion for the two main velocity components; § 8 analyzes the neutral atomic abundances and their implications for cloud core depletions and for ionization balance; and § 9 summarizes the results and describes future plans.

2. THE LINE OF SIGHT

HD 154368 is an O9.5 Iab star at a distance of ~ 800 pc, as determined from its photometry and absolute magnitude. The star lies in a region of extensive obscuration at $l = 350°0$, $b = +3°2$ near the Sco OB1 association (Blades & Bennewith 1973). The gas in this direction has been observed through narrow self-absorption features in H I 21 cm profiles (e.g., Riegel & Crutcher 1972) and through optical absorption lines of Na I toward bright stars in the region (e.g., Crawford, Barlow, & Blades 1989). The main H I and Na I absorption occurs at a heliocentric velocity near $V_{helio} = -3.26$ km s^{-1} corresponding to an LSR velocity of $V_{LSR} = +4.6$ km s^{-1}, while a strong secondary component occurs at $V_{helio} = -20.95$ km s^{-1} ($V_{LSR} = -13.1$ km s^{-1}).

Radio observations have mapped out the distribution of the same gas. The main H I gas seen in the general direction of HD 154368 occurs at $V_{helio} \approx 0$ km s^{-1}, as does the CO emission. Riegel & Crutcher (1972) found this cloud to extend from $l = 345°$ to $l = 25°$ and from $b = -6°$ to $+6°$. Crutcher (unpublished) found that the gas at this velocity actually extends to even higher galactic latitude, appearing in emission when the background H I brightness temperature becomes sufficiently low. At the position of HD 154368, this cold H I cloud is observed in self-absorption at

a velocity of $V_{helio} = -3.26$ km s^{-1}, in agreement with the principal Na I line velocity toward this star. A survey of Na I absorption toward some 49 stars in the same general direction by Crutcher & Lien (1984) argues that this cloud lies only 125 ± 25 pc from the Sun. The line of sight toward HD 154368 is about $14°$ from the core of the very dense ρ Ophiuchi molecular cloud, which has $V_{LSR} = +3.5$ km s^{-1} and a distance of 125 ± 25 pc (de Gues, de Zeeuw, & Lub 1989). Thus, this main component of gas toward HD 154368 is probably not close to the star at all and is likely the outer envelope of the dense molecular clouds only about 125 pc from the Sun.

Another point of view can be found in the discussion of Crawford (1992), who argues that the line of sight toward HD 154368 passes only 15 pc from the Lupus molecular cloud complex, which is centered at $V_{LSR} = +5$ km s^{-1} (Dame et al. 1987), close to the observed velocity of the principal Na I absorption component. Thus, it is possible that the main Na I component (and by inference the strongest UV component in our *HST* data) is associated with outlying gas in the Lupus complex. Whether this is the case, or whether the main absorption component is part of the ρ Oph complex as suggested above, the observed gas is much closer to the Sun than to the star HD 154368 itself.

A strong secondary component along the line of sight toward the star occurs at -20.95 km s^{-1} ($V_{LSR} = -13.1$ km s^{-1}), and it is probably even more local to the Sun. Crutcher (1982) found from an analysis of the velocities of optical interstellar lines toward a number of stars that the Sun is immersed in a coherently moving local interstellar medium whose velocity vector agrees with that of the interstellar wind observed through backscatter of solar Lyman-α and He I λ584 photons. The expected velocity of this local interstellar medium at the position of HD 154368 is $V_{helio} = -22$ km s^{-1}, which corresponds closely to the observed absorption component at $V_{helio} = -20.95$ km s^{-1}. Crutcher (1982) and Crawford et al. (1989) suggested that this material represents the near side of the expanding bubble from the Loop I supernova remnant, which has been accelerated toward the Sun. The lines of sight toward Sco OB1 stars also show strong blueshifted absorption with velocities as negative as -55 km s^{-1}, which Crawford et al. interpret as arising in an expanding shell centered on the OB association. Toward HD 154368 absorption at negative velocities down to -30 km s^{-1} is seen as well, which is probably associated with the same material. For this interpretation to be correct, however, the gas associated with the Loop I supernova remnant would have to be more extended on the sky than previously thought (e.g., Bruhweiler et al. 1980).

3. OBSERVATIONS

3.1. *HST Observations and Data Reduction*

The *HST* data were obtained with the Goddard High Resolution Spectrograph (GHRS), employing a mixture of gratings and observing modes. Observations of spectral features longward of 1800 Å were carried out using the Echelle-B grating and the Large Science Aperture (LSA), which provided a net spectral resolving power of approximately $\lambda/\Delta\lambda = 60,000$. Standard substepping was used in order to reduce fixed-pattern noise due to pixel-to-pixel variations in sensitivity, and the observations were broken up into exposures of 5 minute duration or less, in order to minimize wavelength shifts due to magnetic effects.

The short-wavelength spectra were obtained with grating G160M, which provides a spectral resolution of $\Delta\lambda \approx 0.072$ Å (≈ 14 km s^{-1} at 1500 Å). This was necessary because Echelle-A was unavailable for use at the time of the observations (1992 March). Again, standard substepping was used. In order to maximize the effective resolving power for the G160M spectra, the Small Science Aperture (SSA) was employed, even though this caused considerable loss of throughput due to the spherical aberration of the primary mirror.

Table 1 lists the observations, including central wavelength for each setting, grating and aperture used, wavelength coverage, and exposure time.

The data were reduced following procedures developed by the GHRS Science Team; these procedures are documented by Cardelli, Ebbets, & Savage (1990, 1993). In essence, the individual exposures at each wavelength were wavelength calibrated separately and then co-added to obtain the final spectra. IDL routines were used to determine the optimal shifts from pixel space to wavelength for our substepped data. Calibration lamp exposures were used to verify the wavelength scale, but in all cases we found that the accuracies in the standard wavelengths were within the uncertainties of the calibration lamp lines, so no special recalibration of wavelengths was needed.

The co-added spectra were then maintained in files which were used for the measurement of equivalent widths and subsequent line profile fitting (described below).

3.2. *IUE Observations and Data Reduction*

As a prelude to our *HST* observations of HD 154368, we obtained Guest Observer data on the star using the *IUE* in both high-dispersion and low-dispersion modes. Details of the *IUE* and its operation can be found in Boggess et al. (1978).

We obtained multiple exposures using both the short-wavelength prime (SWP) and long-wavelength prime (LWP) cameras, with the star at different offset positions in the large aperture in order to minimize fixed-pattern noise when the spectra were subsequently co-added. Table 2 lists the exposures obtained for this program.

Initial data reduction was performed by the *IUE* Project at Goddard Space Flight Center, which provided extracted spectra. We then used routines developed at Colorado to shift and co-add the high-dispersion spectra before analysis of the interstellar lines, and to derive extinction curves through star-pair comparison from the low-dispersion spectra. Interstellar atomic column densities were obtained by the curve-of-growth method (e.g., Morton 1975), through use of a software package called MSLAP developed by C. L. Joseph and available at Colorado.

3.3. *Ground-based Observations*

HD 154368 has been studied extensively through absorption-line observations at visible wavelengths, starting with the work of Blades & Bennewith (1973). Below we summarize the available data and present additional observations obtained in the course of this study at two different ground-based observatories: the Anglo-Australian Telescope (AAT) and the European Southern Observatory (ESO).

AAT spectra of the Na D1 line were obtained by one of us (T. P. S.) on 1993 June 1, using the new Ultra High Resolution Facility (UHRF). This instrument is an echelle spectrograph capable of achieving resolving power $R = \lambda/\Delta\lambda = 10^6$ (Crawford et al. 1994; Barlow et al. 1995; Diego et al. 1995). On the night in question, the value of R was measured with a neon laser line to be 9×10^5. Data reduction was straightforward, since each spectrum consisted of a single strip on a CCD image. The cosmic-ray hits were removed with a filtering routine available at the AAT, and the remainder of the reduction (background subtraction, compression into a single row of spectral elements, wavelength assignment, co-addition) was carried out at Colorado using IRAF.

HD 154368 was included in a program to obtain high-resolution profiles of interstellar lines toward several bright stars in the Sco-Oph region. The bulk of the results are still in analysis (Snow 1996). Even though HD 154368 is fainter than the other program targets, the results for the Na I D1 line at 5896 Å are very good. The spectrum (see § 4) obtained after two 30 minute exposures has a signal-to-

TABLE 1
SUMMARY OF GHRS OBSERVATIONS

λ_{cent} (Å)	Range (Å)	Grating	Aperture	Exposure (s)	Number of Exposures	S/N
1161........	1140–1182	G160M	SSA	250	12	10
1220........	1200–1240	G160M	LSA	200	2	25
1241........	1222.7–1258.8	G160M	SSA	250	20	65
1263........	1244.7–1280.8	G160M	SSA	150	33	70
1296........	1278.4–1314.4	G160M	SSA	150	30	100
1336........	1317.9–1353.7	G160M	SSA	300	48	100
1365........	1346.8–1382.6	G160M	SSA	90	67	65
1414........	1396.2–1431.9	G160M	SSA	300	7	100
1706........	1689.4–1724.0	G160M	SSA	300	9	100
1806.7......	1805.9–1807.6	Echelle-B	LSA	300	4	70
2026.1......	2020.9–2031.2	Echelle-B	LSA	300	3	25
2026........	2009.5–2042.8	G160M	SSA	300	3	25
2302.4......	2296.9–2307.7	Echelle-B	LSA	150	15	35
2325.6......	2319.3–2331.9	Echelle-B	LSA	1050	7	85
2334.2......	2327.9–2340.3	Echelle-B	LSA	150	15	75
2360.2......	2354.2–2366.2	Echelle-B	LSA	...	...	...
2366.5......	2360.5–2372.4	Echelle-B	LSA	150	45	65
2369.1......	2363.1–2374.9	Echelle-B	LSA	300	4	40
2582.5......	2576.0–2588.9	Echelle-B	LSA	300	7	140
3078.5......	3069–3087.0	Echelle-B	LSA	150	45	90

TABLE 2

IUE SPECTRA OF HD 154368

Image Number	Resolution	Exposure Time	Exposure Level (DN)[a]	Fine Error Sensor X, Y Coordinates
LWP 18435......	Low	2×4 minutes	C = 14 $\times$, B = 20	$-165, -172; -123, -180$
LWP 20123......	Low	2×17 s	C = 250, B = 34	$-165, -172; -123, -180$
LWP 20124......	Low	2×45 s	C = 4 $\times$, B = 35	$-165, -172; -123, -180$
SWP 39292......	Low	3×40 s	C = 139, B = 18	$-144, -176; -165, -172; -123, -180$
SWP 39293......	Low	40 s	C = 125, B = 18	$-144, -176$
SWP 39294......	Low	2×3 minutes	C = 2.5 $\times$, B = 17	$-165, -172; -123, -180$
LWP 18432......	High	20 minutes	C = 239, B = 59	$-144, -176$
LWP 18433......	High	20 minutes	C = 232, B = 51	$-123, -180$
LWP 18434......	High	20 minutes	C = 223, B = 45	$-165, -172$
LWP 20125......	High	40 minutes	C = 2 $\times$, B = 50	$-144, -176$
LWP 20813......	High	60 minutes	C = 3 $\times$, B = 60	$-123, -180$
LWP 20814......	High	42 minutes	C = 2 $\times$, B = 50	$-165, -172$
SWP 39291......	High	60 minutes	C = 195, B = 61	$-144, -176$
SWP 41364......	High	140 minutes	C = 228, B = 65	$-144, -176$
SWP 41365......	High	70 minutes	C = 195, B = 42	$-165, -172$
SWP 41366......	High	70 minutes	C = 190, B = 42	$-123, -180$
SWP 42074......	High	140 minutes	C = 2 $\times$, B = 65	$-123, -180$
SWP 42075......	High	140 minutes	C = 2 $\times$, B = 60	$-165, -172$

[a] C stands for continuum; B stands for background.

noise ratio S/N $\approx$ 40. It proved to be very useful in determining the velocity structure in the line of sight, which is essential for analyzing the lines observed with *HST*. High-resolution ($R = 10^5$) observations of the Ca II K $\lambda3933$ line have been presented by Crawford (1992), which will be important for comparison.

Several lines of the interstellar C_2 molecule in the $A-X$ Phillips system at 8750 Å have been detected toward HD 154368 at ESO by van Dishoeck & de Zeeuw (1984) at $V_{\rm helio} \approx -3$ km s^{-1}. The measured C_2 rotational population provides useful information on the physical parameters (temperature and density) in the molecular component. The inferred parameters are $T_{\rm kin} \approx 25$ K and $n = n(H) + n(H_2) \approx 225$ cm^{-3}. This cloud is predominantly molecular; therefore, if $n(H) \approx 0.5n(H_2)$, then the total density of hydrogen nuclei is estimated to be $n_H = n(H) + 2n(H_2) \approx 350$ cm^{-3}.

The violet $B-X$ (0, 0) system of CN has been observed extensively by Blades (1978), Palazzi et al. (1990), Gredel, van Dishoeck, & Black (1991), and Roth & Meyer (1995). The CN $A-X$ (0, 0) red system has been detected by van Dishoeck & Black (1989). The CN data have been analyzed in detail by Gredel et al. (1991) and imply an excitation temperature $T_{\rm ex} = 2.86$ K. The best fit is obtained with two closely spaced components that have a small b (= 0.43 km s^{-1} each) and a velocity separation of 0.65 km s^{-1}. This fit was based on the observed CO 1–0 emission profile, although in Paper II we explore an alternative fit that invokes self-absorption instead of a velocity separation. The inferred excitation temperature can be used to constrain the electron density in the molecular component, $n_e \approx$ 0.05–0.15 as shown by Black & van Dishoeck (1991). A slightly different analysis has been carried out by Roth & Meyer (1995).

Several lines of CH and CH$^+$ have been detected by van Dishoeck & Black (1989) and Gredel et al. (1993). The CH observations are important because they can be used to infer the total amount of H_2 along the line of sight, which is needed to determine the atomic depletions. The measured column density of CH$^+$ (2×10^{13} cm^{-2}) is comparable to that found for the well-studied line of sight toward ζ Oph.

Lines of additional neutral atomic species at visible wavelengths have been obtained at ESO using the 1.4 m Coudé Auxiliary Telescope (CAT) equipped with the Coudé Echelle Spectrometer (CES). The data were obtained with the CCD number 9 array at a resolving power $R \approx 60,000$ and were reduced in Leiden using the IRAF package. The resulting detections and upper limits are included in Table 5. In addition, observations of the Na I $\lambda3302$ line have been presented by Crawford (1992). These data are useful in constraining further the ionization balance in the cloud.

The HD 154368 cloud is thick enough that molecular emission lines at millimeter and submillimeter wavelengths are detectable. ^{12}CO 1–0, 2–1, and 3–2 and ^{13}CO 1–0 data toward the star have been presented by van Dishoeck et al. (1991) and have been used to constrain the CO column density and H_2 density in the molecular component. The analysis of the CO excitation confirmed the relatively low density $n(H_2) \approx 300$ cm^{-3} found from the C_2 absorption-line data. The CO emission-line data obtained in beams of diameter 20″–60″ will be compared with the ultraviolet absorption-line observations of CO in a narrow beam (defined by the angular size of the star) in Paper II. The CO 1–0 emission has been mapped over a 30′ × 30′ region around the star by Gredel, van Dishoeck, & Black (1994). The resulting distribution is rather featureless with no apparent physical influence of the star, consistent with the notion that the star is not located close to the cloud but well behind it.

Searches for emission lines of other molecules have been made by Palazzi et al. (1990) and Gredel et al. (1991, 1994). Only very weak CN emission at 2.64 mm has been detected, but no CS, C_2H, HCO$^+$, or HCN lines have been found.

4. THE ULTRAVIOLET EXTINCTION CURVE

The ultraviolet extinction curve for HD 154368 was derived from the low-dispersion *IUE* data described above. The star comparison method requires a comparison spectrum for a star having similar intrinsic flux distribution, which is divided into the reddened star spectrum and normalized to $E(B-V)$ or to the total extinction A_V. In our case, we followed the convention established by earlier

studies of UV extinction (e.g., Savage & Mathis 1979; Seaton 1979) and normalized to A_V.

The comparison star of choice was HD 188209, a lightly reddened O9 Ia star. In order to carry out the comparison with HD 154368, it was first necessary to remove the extinction from (i.e., to "deredden") the spectrum of HD 188209. This is commonly done by applying the "average" interstellar extinction curve (Savage & Mathis 1979; Seaton 1979), but in view of the many extinction curves that deviate significantly from this average, this procedure can introduce significant error. Instead, we used a star whose UV extinction had been derived by an iterative process in which intrinsic stellar flux distributions are derived as functions of spectral type and luminosity class, so that the extinction can be deduced independent of any assumptions about average curves. Thus, we used the intrinsic flux distribution for HD 188209 as derived by Cardelli, Sembach, & Mathis (1992). This method revealed that we would have underestimated the UV extinction toward HD 154368, if we had dereddened HD 188209 using the average interstellar extinction curve.

The derived interstellar extinction toward HD 154368 from 3 to 8.7 μm^{-1} (3300–1150 Å) is shown in Figure 1a. We have fitted this curve following the parameterization of Fitzpatrick & Massa (1986, 1988, 1990), which yields six parameters as follows: $\gamma = 1.15\ \mu m^{-1}$; $\lambda_0^{-1} = 4.581\ \mu m^{-1}$; $c_1 = -0.01$; $c_2 = 0.680$; $c_3 = 4.419$; and $c_4 = 0.807$, based on a normalization of the extinction curve to $E(B-V)$, as

was the convention adopted by Fitzpatrick & Massa. These parameters can be converted to those based on normalization to A_V by $a_1 = c_1/(R + 1)$; $a_2 = c_2/R$; $a_3 = c_3/R$; and $a_4 = c_4/R$ (Mathis & Cardelli 1992). The central wavelength and bump width parameters γ and λ_0^{-1} are unaffected by the normalization to A_V.

The dashed line in Figure 1a represents the predicted extinction curve for a value of the ratio of total to selective extinction of $R_V = 3.1$ (Cardelli, Clayton, & Mathis 1989, hereafter CCM). It was shown by CCM that most extinction curves (near-IR through UV) can be represented by a universal function with a single scaling parameter R_V, to the extent that the shape of the UV extinction can be predicted from R_V and vice versa. The derived HD 154368 curve deviates no more than 1 σ from the predicted CCM curve (see Fig. 1b); therefore, it appears that HD 154368 conforms to the general pattern.

Cardelli & Clayton (1991) and Mathis & Cardelli (1992) have shown that the scatter around the CCM relationship is larger in the UV that can be expected from random errors, and that, therefore, some stars deviate significantly from this relationship. Cardelli & Clayton (1991) describe systematic deviations from the CCM relation that correlate with environment, e.g., bright nebulae versus dark clouds. Although the deviations of the HD 154368 curve are smaller than 1 σ, they are consistent with the dark cloud pattern, as illustrated in Figure 1c. Thus, the interstellar medium toward this star has a component of "dark cloud" dust, but this is not dominant.

5. THE VELOCITY STRUCTURE

The major uncertainty in analyzing strong interstellar absorption lines arises from the effects of unresolved velocity structure in the line of sight upon the saturation of the absorption. Lines that are saturated but not damped (i.e., that lie on the flat portion of the curve of growth) are intrinsically difficult because their equivalent widths are insensitive to column density; thus, there is always the possibility that weak velocity components lie hidden within the absorption due to strong components. Ideally, it is desirable to have sufficient spectral resolving power to unravel the velocity structure, but in practice even the high-resolution modes of the GHRS (at best 3.5 km s^{-1} resolution) fall short of what is needed to distinguish interstellar features whose widths and separations are of the order of 1–3 km s^{-1}. It is possible to make some progress by the use of profile-fitting techniques which in effect allow the separate components to be deconvolved, but in the absence of good information on the velocity structure to begin with, large ambiguities remain.

Fortunately, we have been able to obtain some information at very high resolving power: the Na I data obtained using the UHRF on the AAT. Figure 2 shows the profile of the Na I D1 feature, along with the fit we were able to derive and indicators of the separate components. The fit was achieved using the program FITS4, a descendant of a program originally developed by Vidal-Madjar et al. (1977), which has since been modified to work on UNIX-based workstations. The fit included the hyperfine structure of the Na I line, which is resolved (but not seen clearly because of the overlapping of velocity components). An independent check was performed with a profile synthesis program developed by one of us (J. H. B.), and good agreement was found between the two analyses.
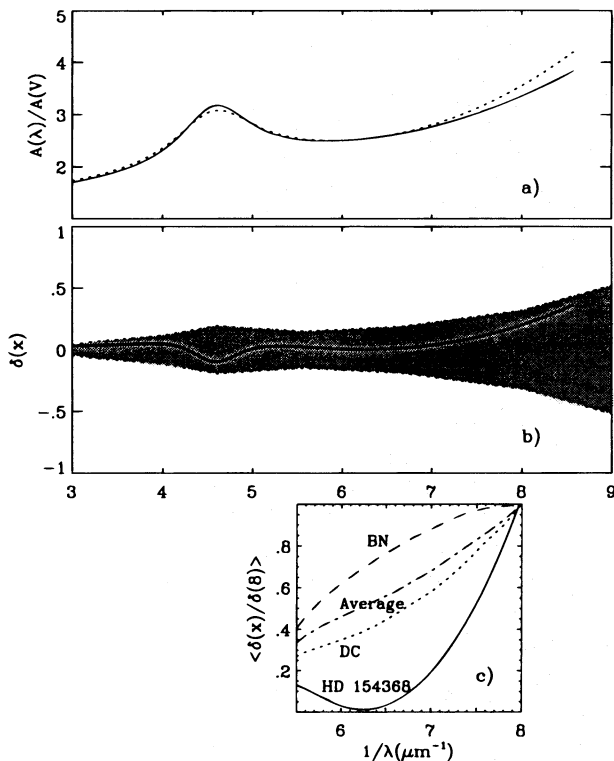

FIG. 1.—The UV extinction curve toward HD 154368. (a) The derived extinction curve (*solid line*), with a predicted curve from Cardelli et al. (1989) based on the value $R_V = 3.1$. (b) The deviations of the observed curve from the predicted curve, with shading to indicate the $\pm 1\ \sigma$ envelope. (c) Comparison of the small deviation seen for HD 154368 with the types of deviations seen in various environments. The general conclusion in the text is that the curve for HD 154368 fits the standard behavior found by Cardelli et al. rather well, but that the small deviations seen are in the sense expected for dark cloud material.
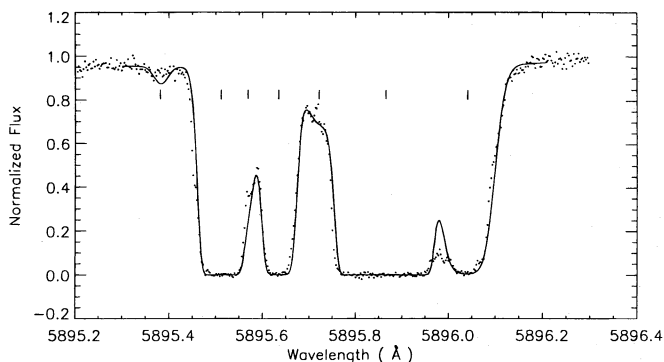
FIG. 2.—The Na I D1 line profile. Plus signs are the observed data points from the UHRF (see text), and the solid line represents our best fit, using seven velocity components which are indicated by vertical marks along the continuum level. The results of the profile fitting are presented in Table 3.

The majority of the seven components needed to achieve a good fit have well-defined values of both column density, b-value, and velocity. Only within the strongest component, centered at -3.26 km s^{-1}, is there significant ambiguity due to saturation. Based on experiments with varying the column densities and b-values, we estimate that for the six weaker components the column densities are accurate to within 20%, while for the strongest component the uncertainty is of order 50%. Approximately 96% of all the Na I is in the -3.26 km s^{-1} component; most of the rest (about 2.4% of the total) is in the -20.95 km s^{-1} component.

The b-values are thought to be accurate to within 0.2 km s^{-1}, based on experiments conducted by varying the parameters until the fit became unacceptable. For the strongest component, the required b-value (2 km s^{-1}) is larger than for the weaker components. We attempted to fit the strong line with two narrow features ($b = 1.0-1.5$ km s^{-1}, separated by 1 km s^{-1}), but no reasonable fit could be

found. The data are therefore consistent with a single, $b = 2$ km s^{-1} component.

The relative velocities, again with the exception of the strong -3.26 km s^{-1} component, are accurate to approximately 0.1–0.2 km s^{-1}. The absolute velocity scale was derived from the calibration lamp lines observed at the time of the UHRF observations and was verified by the additional geocentric wavelength calibration offered by nearby atmospheric water vapor lines. The main components match well with those observed in Ca II by Crawford (1992), both in absolute velocity and in velocity separation.

Table 3 summarizes the components needed to fit the Na I line. These values for velocity, b, and relative column density were then used as starting points for the fits of the ultraviolet lines observed with the GHRS. Errors are difficult to quantify because of the possible ambiguities of the fits in some cases, but experimentation with the fit to the Na I line suggests that for the two main components (at -3.26 and -20.95 km s^{-1}), the values listed in Table 3 are accurate to within 10%.

We compared our fit to the Na I line with that obtained by Crawford (1992) for his high-resolution ($R = 100,000$) data on Ca II toward HD 154368, with results shown in Table 4. The Ca II data show only five clear components, as opposed to the seven that were required to allow a good fit to Na I. These five (at -27.6, -20.9, -14.4, -4.3, and $+6.8$ km s^{-1}) coincide closely with Na I components, but the relative column densities are different. Where Na I shows some 96% of the total column density in the -3.26 km s^{-1} component and most of the rest in the -20.95 km s^{-1} component, Ca II shows a more even distribution across four of the five components, although the gas at -3.26 km s^{-1} still contains most of the column density; approximately 53%. The b-values for Ca II are distinctly higher than for Na I, perhaps not a surprising result in view of the fact that Ca II is a more populous ionization state than Na I, and therefore it is likely to be more widely distributed within each cloud along the line of sight. It has been known for a long time that the Na I/Ca II abundance ratio varies greatly from place to place (Spitzer & Routly 1952).

A slightly different fit is possible, in which the -3.26 km s^{-1} component is assumed to be so strong that it has damping wings, thus eliminating the need for a component at -10.5 km s^{-1}. The column density of the -3.26 km s^{-1} component in this case would increase by about 2%, which would have only a minor impact on our later discussions of depletions.

6. ATOMIC COLUMN DENSITIES

An assortment of methods was used to determine column densities of the various species observed from the ground and from space. The database employed in this analysis is presented in Table 5, which lists the wavelengths, oscillator strengths, and observational data (equivalent widths and uncertainties) for interstellar absorption lines in the spectrum of HD 154368. The table includes lines observed with the *HST, IUE*, and various ground-based observatories (primarily the European Southern Observatory).

In the following subsections, we describe the derivation of column densities for different species and the methods used.

6.1. *Hydrogen*

The atomic hydrogen column density was derived following the formalism of Bohlin (1975), in which the profile is

TABLE 3

ANALYSIS OF THE Na I PROFILE

Velocity (km s^{-1})	N (Na I) (cm^{-2})	b-value (km s^{-1})	Percent of N_{Total}
-27.7	2.0(10)	1.0	0.0048
-20.95	1.0(13)	1.4	2.4
-18.2	2.0(11)	1.0	0.048
-14.75	3.0(12)	1.2	0.72
-10.5	1.2(11)	2.0	0.029
-3.26	4.0(14)	2.1	96.2
$+5.62$	2.5(12)	2.2	0.60

TABLE 4

COMPARISON OF THE Na I AND Ca II PROFILES[a]

Velocity (km s^{-1})	Percent Na I	Percent Ca II	Ca II Velocity (km s^{-1})	b-value Na I (km s^{-1})	b-value Ca II (km s^{-1})
-27.7	0.0047	2.6	-27.6	1.0	3.0
-20.95	4.7	12	-20.9	1.1	2.5
-18.2	0.07	...	...	1.0	...
-14.75	0.7	16	-14.4	1.2	2.8
-10.5	0.047	...	...	1.5	...
-3.26	94	52	-4.3	2.1	3.5
$+5.62$	0.94	17	$+6.8$	2.4	3.5

[a] Results for Ca II are from Crawford 1992.

TABLE 5
EQUIVALENT WIDTHS

Species	λ (Å)	f	W_λ (mÅ)	Mean Error (mÅ)	Observatory	Mode	References
Li I	6707.761	0.465	26	1.7	ESO	...	
C II]	2325.403	5.8E(−8)	≈1.1	0.64	HST	Echelle-B	
	2324.214	2.8E(−9)	≤1.3	0.64	HST	Echelle-B	
C II	1334.5323	0.1288	364	7	HST	G160M	
			377	43	IUE	...	
C II*	2326.113	5.26E(−8)	≤1.3	0.64	HST	Echelle-B	
	1335.7077	0.1159	230	7	HST	G160M	
			201	29	IUE	...	
O I]	1355.5977	1.25E(−6)	16.9	6.8	HST	G160M	
O I	1302.1685	0.04887	323	6	HST	G160M	
			?	49	IUE	...	
Na I	3303.368	8.836E(−3)	76	3	...	...	1
	3302.978	4.417E(−3)	93	3	...	...	1
Mg I]	4571.0957	2.65E(−6)	≤1.5	...	ESO	...	
Mg I	2852.9642	1.83	372	16	IUE	...	
	2026.4762	0.1154	132	8	HST	Echelle-B	
			131	2?	IUE	...	
	1827.9351	0.0245	77	16	IUE	...	
	1707.061	4.142E(−3)	37	2	HST	G160M	
	1683.412	2.485E(−3)	15	3?	IUE	...	
Mg II	2803.531	0.3057	664	18	IUE	...	
	2796.352	0.6129	717	21	IUE	...	
	1240.3947	1.337E(−4)	41	3	HST	G160M	
	1239.9253	2.675E(−4)	63	4	HST	G160M	
Al I	3944.0061	0.1154	≤4.0	...	ESO	...	
	2372.7944	4.045E(−3)	≤2.6	3.3	HST	Echelle-B	
	2367.7762	0.1211	≤2.6	1.3	HST	Echelle-B	
Al II	1670.7874	1.833	276	22	IUE	...	
Si I	1845.5202	0.2291	27	7	IUE	...	
Si II]	2335.123	4.25E(−6)	4.0	2.0	HST	Echelle-B	
Si II........	1808.0126	2.08E(−3)	191	1	HST	Echelle-B	
			192	12	IUE	...	
	1526.7066	2.10E(−3)	281	30	IUE	...	
	1304.3702	0.088	227	4	HST	G160M	
			211	25	IUE	...	
Si III	1206.500	1.696	520	6	HST	G160M	
P II	1301.874	0.0309	38	2	HST	G160M	
S I	1807.3113	0.1105	70	1	HST	G160M	
	1473.9943	0.0730	51	16	IUE	...	
	1425.0299	0.1918	91	6	HST	G160M	
	1316.5425	0.0345	57	20	IUE	...	
	1295.6531	0.1235	60	3	HST	G160M	
			34	20	IUE	...	
	1270.7804	0.0551	32	3	HST	G160M	
S II	1259.519	0.01624	192	1	HST	G160M	
			207	32	IUE	...	
	1253.811	0.01088	181	6	HST	G160M	
			225	75	IUE	...	
	1250.584	5.453E(−3)	142	4	HST	G160M	
			167	37	IUE	...	
Cl I	1347.2396	0.1186	86	4	HST	G160M	
			87	21	IUE	...	
K I	4047.213	3.042E(−3)	1.0	0.5	ESO	...	
	4044.143	6.089E(−3)	2.4	0.5	ESO	...	
Ca I	4226.728	1.61	6.5	1.0	ESO	...	2
CCa II......	3933.663	0.6346	282	...	...	...	1
Ca II........	3968.468	0.3145	161	...	ESO	...	2
Ti I	3635.463	0.2188	≤3.0	...	ESO	...	
Ti II	3073.877	0.1091	11.1	0.8	HST	Echelle-B	
V I..........	4577.174	0.021	≤1.5	...	ESO	...	
	3855.362	0.062	≤1.0	...	ESO	...	
Cr I.........	4254.332	0.111	≤2.0	...	ESO	...	
Mn I	4030.753	0.061	≤1.0	...	ESO	...	
Mn II.......	2606.462	0.1927	210	18	IUE	...	
	2594.499	0.2710	248	15	IUE	...	
	2576.877	0.3508	257	1	HST	Echelle-B	
			265	17	IUE	...	
	2305.714	1.239E(−3)	3.2	0.8	HST	Echelle-B	

TABLE 5—*Continued*

Species	λ (Å)	f	W_λ (mÅ)	Mean Error (mÅ)	Observatory	Mode	References
Fe I.......	3859.9113	0.02166	2.2	?	ESO	...	
	3719.9343	0.04119	≤5.0	...	ESO	...	
	2298.8772	0.04303	≤3.5	...	HST	Echelle-B	
Fe II	2600.1729	0.2239	441	16	IUE	...	
	2586.6500	0.06457	411	16	IUE	...	
	2382.765	0.3891	454	37	IUE	...	
	2374.4612	0.02818	299	2	HST	Echelle-B	
			341	35	IUE	...	
	2367.5905	2.118E(−4)	≤2.6	...	HST	Echelle-B	
	2344.214	0.1097	337	65	IUE	...	1
	1608.4511	0.06194	189	15	IUE	...	
Co I	2365.782	0.01072	≤2.9	...	HST	Echelle-B	
Ni II	1741.549	0.1035	49	7	IUE	...	
	1709.600	0.06884	48	3	HST	G160M	
	1370.132	0.1309	51	17	IUE	...	
	1317.217	0.1458	33	14	IUE	...	
Zn II......	2026.136	0.4135	347	8	HST	Echelle-B	

REFERENCES.—(1) Crawford 1992; (2) Gredel et al. 1993.

assumed to be dominated by natural broadening, and the column density is found iteratively by varying trial values of $N(H)$ until a value is found which best restores the continuum when the spectrum is multiplied by exp $(+\tau)$, where τ is the optical depth as a function of wavelength.

For HD 154368 this leads to a value for atomic hydrogen of $N(H) = 1.0 \times 10^{21}$ cm^{-2}, with an allowed range from 0.9 to 1.05×10^{21} cm^{-2}. This column density is significantly larger than values found for less reddened diffuse-cloud stars (e.g., ζ Oph; Morton 1974, 1975), but it is lower than expected from a straightforward extrapolation of the $N(H)$ versus $E(B-V)$ correlation. This is an indirect indication that a significant fraction of the hydrogen must be molecular. The estimated value of $N(H_2)$ is discussed below and in Paper II.

6.2. *Other Species: Profile Fitting*

The column densities of atoms and ions other than hydrogen were derived using the FITS4 program and our own program, in the same fashion as described earlier for fitting the Na I line. For the GHRS data, however, the velocity resolution was insufficient to allow an unambiguous and independent derivation of the velocity structure, so we adopted the velocity component separations found from the Na I analysis. We constrained only the velocities, not the relative column densities or the b-values, thus allowing for the likely situation that different species have different distributions from cloud to cloud along the line of sight. The atomic data were taken from the compilation by Morton (1991a, b), except as noted.

Figure 3 shows some example fits for profiles obtained with Echelle-B, which had an effective resolving power of $R = \lambda/\Delta\lambda = 60,000$ at the time of our observations. All seven of the components derived from the Na I analysis were included in each fit, and in most cases they were needed in order to obtain a satisfactory match. The lines observed using grating G160M were also analyzed by profile fitting, but the results were less secure, in view of the lower resolving power ($R \approx 20,000$ at $\lambda \approx 1500$ Å) afforded by this grating.

For each species, only one line was fitted independently. An exception is formed by the Mg II doublet at 1240 Å,

where the two lines were fitted simultaneously. Once a satisfactory fit was achieved, then the resulting column densities and b-values were used to calculate synthetic profiles for the other lines of each species, as a consistency check. In some cases, adjustments were made in order to find a solution that was satisfactory for all observed lines, but in most cases this was not necessary because the fit derived for the first line was consistent with the others as well.

Table 6 lists the results of the profile fitting, for lines having sufficient data quality to allow an independent derivation of the column densities for individual velocity components. Most of these cases were Echelle-B observations, but some of the G160M data also proved to be of sufficient quality. The individual b-values and column densities are listed, together with the totals for each line.

Some general comments regarding the accuracy of the results are in order. First, obviously the Echelle-B data were far more useful and led to more definitive results than did the G160M spectra. For example, the fits to Si II $\lambda1808$ and Zn II $\lambda2026$ have rather small uncertainties for all seven velocity components, whereas the fits for others such as S II $\lambda\lambda1250$, 1253, 1259, and C II $\lambda1334$ all have rather large uncertainties. The errors in the profile parameters for lines observed with Echelle-B are comparable to those quoted above for the Na I profile: for the weaker components the column densities appear to be accurate to within 20%, whereas for the strongest component (at $V_{helio} = -3.26$ km s^{-1}) the uncertainty may be as large as 50%. For lines observed with grating G160M the uncertainties are larger: for an individual profile the error in derived column density in the -3.26 or -20.95 km s^{-1} components can be as large as a factor of 2–5. A few particularly important cases are discussed below.

C II.—The fit to the $\lambda1334$ line was uncertain because the line is very strong, and because it was observed only at moderate resolution, with grating G160M. For the two strongest components, at -3.26 and -20.95 km s^{-1}, the uncertainties based on this fit alone are nearly 2 orders of magnitude. Only if we consider also the measurement of the semiforbidden C II] line at 2325 Å do we find some useful constraints on the C II column density. This spectral region is shown in Figure 4. A dip appears at the appropriate
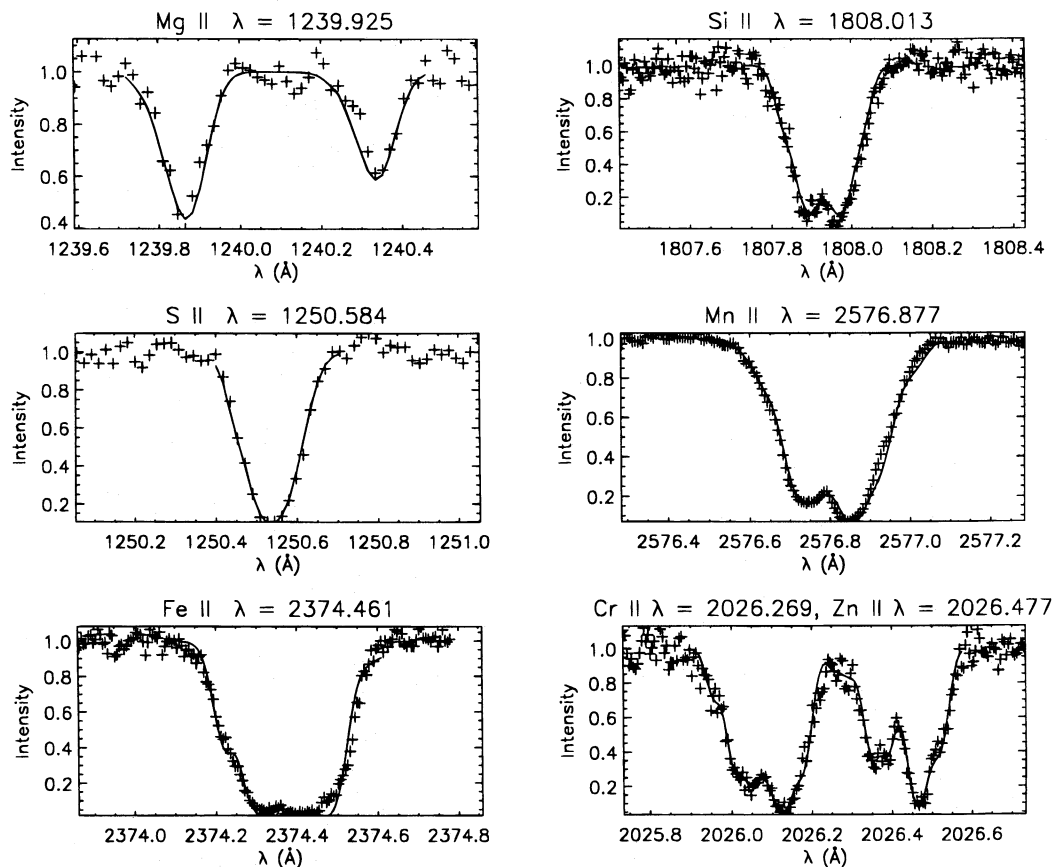
Fig. 3.—Example fits to *HST* data. The observed spectra are indicated by plus signs and the fits by solid lines. Two of the profiles (Mg II λλ1239, 1240 and S II λ1250) were observed with grating G160M, while the rest were observed with Echelle-B. Results of all the profile fits are given in Table 6.

location, but only at the 2 σ level, and we do not claim a clear detection. Nevertheless, we were able to extract useful limit information. By removing a linear baseline (shown in the figure) and then performing a least-squares fit to the line, we derive an equivalent width of $W_\lambda = 11 \pm 6.4$ mÅ. Combined with our adopted f-value of 5.80×10^{-8} (based on the lifetime measurement of Fang et al. 1993, scaled for the relative transition probabilities within the multiplet from Lennon et al. 1985), this yields a column density of $N(C^+) = 4 \times 10^{17}$ cm^{-2}. If the C II absorption is distributed across the velocity components in the same way as Ca II, then this represents 52% of the total C$^+$ column density, leading to $N(C^+) \approx 8 \times 10^{17}$ cm^{-2}. We also attempted a profile fit, using the velocity structure seen in the Ca II K line, with the result shown in the bottom panel of Figure 4. The dashed lines show the behavior for C$^+$ column densities of 4×10^{17} cm^{-12} and 1×10^{18} cm^{-2}, indicating that the probable true value is within this range. We adopt a final value for the C II column density of $N(C\,II) \approx 7 \pm 3 \times 10^{17}$ cm^{-2}.

O I.—We observed two O I lines with grating G160M in each case. The weak intersystem line at 1355.574 Å appeared at the 2.5 σ level (Fig. 5). A single Gaussian fit to the observed feature has $W_\lambda = 17 \pm 7$ mÅ. We also computed simulated profiles, using the velocity structure derived from the Ca II profile, to find the extremes of acceptable fits to the line; these synthetic profiles are shown in the figure. From these fits we derive limits on the O column

density, yielding $N(O) = (1.2 \pm 0.3) \times 10^{18}$ cm^{-2}. To check this for consistency, we calculated simulated profiles for the strong O I line at 1302 Å (see Fig. 6). The profile shown was calculated for the column density derived from the λ1355 line and provides a good fit, so we conclude that the column density cited above is valid.

Si II.—The 1808 Å line was observed with Echelle-B, and the high-quality spectrum that resulted allowed a fit with relatively high confidence. The results are in Table 6, which gives a total column density $N(Si\,II) \approx 5 \times 10^{15}$–$5 \times 10^{16}$ cm^{-2}. We also had data on the semiforbidden line at 2335 Å and detected it at the 4 mÅ level (Fig. 7), marking only the second known detection of this feature (it was also seen in the spectrum of ζ Oph; see Cardelli et al. 1994). Interpretation of this line led us to reevaluate and summarize the current best values for Si II f-values (see Appendix A), leading to an adopted value for the λ2335 line of $f = 4.25 \times 10^{-6}$ (Calamai, Smith, & Bergeson 1993). This oscillator strength implies a Si$^+$ column density of 1.9×10^{16} cm^{-2}, which we assume represents mostly the -3.26 km s^{-1} component. If this cloud contains 82% of the Si$^+$ in the line of sight, as derived from fitting the λ1808 line, then the total S$^+$ column density is $N(Si^+) \approx 2.3 \times 10^{16}$ cm^{-2}. This is consistent with the results of the fit to the λ1808 line (which was calculated using a revised f-value, based on Bergeson & Lawler 1993).

S II.—The fit was done independently for the λ1250 line, but the result was then checked by comparing synthetic and

TABLE 6

RESULTS OF PROFILE FITTING

Species	λ (Å)	$V_{\rm Helio}$ (km s^{-1})	log N (cm^{-2})	b (km s^{-1})	log $N_{\rm Total}$ (cm^{-2})
C II.....	1334.5233	−27.87	14.2–16.8	2.5	16.15–18.4
		−20.95	15.2–18.0	2.5	...
		−18.2	15.2–15.8	2.5	...
		−14.75	15.0–15.6	2.3	...
		−10.5	14.0–14.6	1.5	...
		−3.26	16.0–18.1	2.5	...
		+5.62	15.0–17.0	5.0	...
Mg I ...	2026.4762	−27.87	12.1–12.7	1.0	14.19–14.79
		−20.95	13.0–13.6	1.1	...
		−18.7	...	...	...
		−14.75	12.0–12.6	1.0	...
		−10.5	12.7–13.3	1.2	...
		−3.26	14.1–14.7	2.1	...
		+5.62	12.8–13.4	2.4	...
Mg II...	1239.9253	−27.87	14.4–15.0	1.1	16.31–16.91
	1240.3947	−20.95	15.0–15.6	1.2	...
		−18.7	...	...	...
		−14.75	15.2–15.8	1.3	...
		−10.5	...	...	...
		−3.26	16.2–16.8	4.3	...
		+5.62	13.4–14.0	2.5	...
Si II	1808.0126	−27.87	14.0–14.6	1.0	15.7–16.7
		−20.95	15.0–16.0	1.1	...
		−18.7	13.6–14.2	1.0	...
		−14.75	14.6–15.2	1.2	...
		−10.5	14.2–14.8	1.5	...
		−3.26	15.7–16.7	2.1	...
		+5.62	...	...	...
S I	1807.3113	−27.87	11.7–12.3	1.0	13.5
		−20.95	12.6–13.2	1.1	−14.1
		−18.2	...	...	...
		−14.75	11.9–12.5	1.2	...
		−10.5	12.1–12.7	1.5	...
		−3.26	13.3–13.9	2.1	...
		+5.62	12.3–12.9	2.4	...
S II	1250.584	−27.87	14.4–15.0	1.1	16.03–15.63
		−20.95	15.1–15.7	1.9	...
		−18.2	14.2–14.8	1.0	...
		−14.75	15.2–15.8	2.3	...
		−10.5	14.0–14.6	1.5	...
		−3.26	15.8–16.4	2.6	...
		+5.62	15.2–15.8	2.5	...
Ti II	3073.877	−27.87	...	...	...
		−20.95	11.3–11.9	1.0	...
		−18.2	...	...	...
		−14.75	10.9–11.5	2.1	...
		−10.5	...	...	...
		−3.26	11.7–12.3	1.1	...
		+5.62	...	...	...
Mn II...	2576.877	−27.87	12.7–13.3	1.1	13.60–14.80
		−20.95	13.0–13.6	1.2	...
		−18.2	11.5–14.1	1.0	...
		−14.75	12.8–13.4	1.2	...
		−10.5	12.0–12.6	2.1	...
		−3.26	13.7–14.3	2.1	...
		+5.62	12.3–12.9	2.5	...
Fe II....	2374.4612	−27.87	14.3–14.9	1.0	15.56–16.16
		−20.95	14.8–15.4	1.1	...
		−18.2	13.4–14.0	1.0	...
		−14.75	14.4–15.0	1.2	...
		−10.5	13.6–14.2	1.5	...
		−3.26	15.3–15.9	2.1	...
		+5.62	14.6–15.4	2.5	...
Ni I	320.031	−27.87	...	...	...
		−20.95	10.1–10.7	2.1	...
		−18.2	...	...	...
		−14.75	10.0–10.6	1.2	...
		−10.5	...	...	...
		−3.26	10.5–11.1	2.1	...
		+5.62	...	...	...

TABLE 6—Continued

Species	λ (Å)	$V_{\rm Helio}$ (km s^{-1})	log N (cm^{-2})	b (km s^{-1})	log $N_{\rm Total}$ (cm^{-2})
Ni II ...	1804.473	−27.87	...	...	...
		−20.95	12.8–13.4	1.2	...
		−18.2	...	...	...
		−14.75	12.5–13.1	1.2	...
		−10.5	...	...	...
		−3.26	13.4–14.0	2.1	...
		+5.62	11.4–12.0	2.5	...
Zn II...	2026.136	−27.87	11.8–12.4	1.0	14.02–14.62
		−20.95	12.9–13.5	1.1	...
		−18.2	11.3–11.9	1.0	...
		−14.75	12.8–13.4	1.2	...
		−10.5	12.1–12.7	1.5	...
		−3.26	13.9–14.5	2.1	...
		+5.62	12.4–13.0	2.5	...

observed profiles for the λ1253 and λ1259 lines as well. The match was very good indeed; experiments with varying the column densities convinced us that the derived values (Table 6) are accurate to within a factor of 2.

Ni I, Ni II.—The detection and analysis of Ni I is, as far as we know, unprecedented. The line at 2320 Å is weak, but it was detected with high S/N (≈ 85), and an unambiguous fit was found. The lack of saturation in the line helped reduced errors due to unseen blended components, but this was compensated for by the weakness of the line and the correspondingly larger relative uncertainty due to photon statistics.
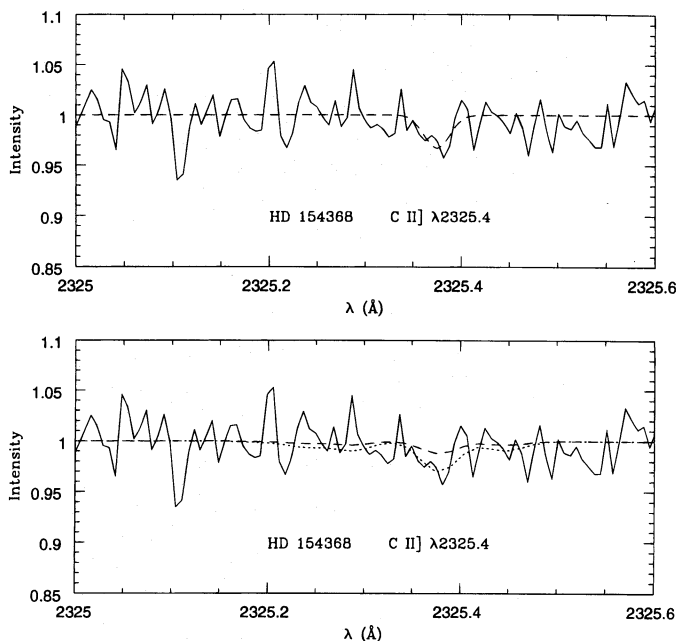

FIG. 4.—*Top*: A least-squares fit of a single Gaussian (*dashed curve*) to the observed spectrum (*solid curve*) in the vicinity of the C II] λ2325 line. The fitted feature is at $V_{\rm helio} = -3.7 \pm 1.7$ km s^{-1} and has an equivalent width $W_\lambda = 1.1 \pm 0.64$ mÅ ($1\ \sigma$). This yields a column density of $N({\rm C}^+) = 4 \times 10^{17}$ cm^{-2} in the main velocity component. In the Ca II velocity model, this component has a fraction 0.52 of the total column density, suggesting a total $N({\rm C}^+) = 8 \times 10^{17}$ cm^{-2}. *Bottom*: Two simulated spectra computed for the Ca II velocity model with total column densities of $N({\rm C}^+) = 4 \times 10^{17}$ cm^{-2} (*dashed curve*) and 1×10^{18} cm^{-2} (*dotted curve*).
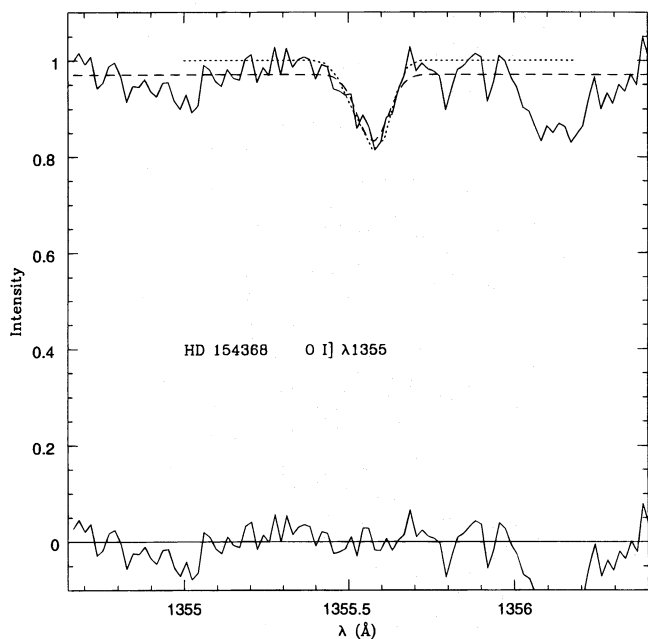
FIG. 5.—The spectrum in the vicinity of the O I] $\lambda 1335.6$ line is shown as a solid curve. The continuum level is difficult to ascertain. The dashed curve is a Gaussian profile that has been fitted by least-squares to the observed spectrum: this profile has an equivalent width of $W_\lambda = 17 \pm 7$ mÅ and a center at $V_{\rm helio} = -5.2 \pm 3.1$ km s^{-1}. The residuals of the Gaussian fit are displayed at the bottom of the figure. The uppermost, dotted curve is a simulated profile for the Ca II velocity model, for which the total column density is $N({\rm O}) = 1.4 \times 10^{18}$ cm^{-2}. The equivalent width of the simulated feature is $W_\lambda = 25.0$ mÅ, which is just barely beyond the 1 σ error limit for the fitted Gaussian. A column density $N({\rm O}) \geq 1.5 \times 10^{18}$ cm^{-2} will produce a feature with a central depth noticeably deeper than observed. A curve of growth computed for the Ca II velocity model yields $N({\rm O}) = 9.0 \times 10^{17}$ cm^{-2} at the lower bound on W_λ; therefore, we adopt $N({\rm O}) = (1.2 \pm 0.3) \times 10^{18}$ cm^{-2}.
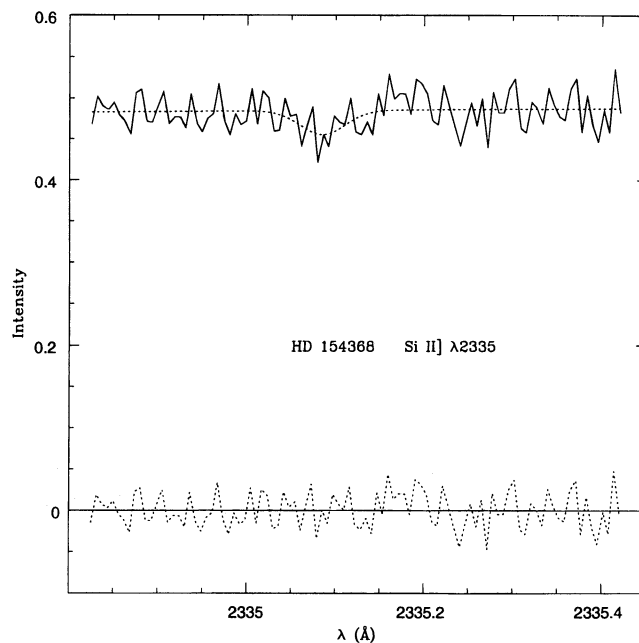
FIG. 7.—The spectrum in the vicinity of the Si II] $\lambda 2335$ line is shown as the solid curve. A least-squares Gaussian fit (*upper dotted curve*) reveals a feature at $V_{\rm helio} = -4.9 \pm 1.2$ km s^{-1} with an equivalent width $W_\lambda = 4.0 \pm 2.0$ mÅ. The residuals of the fit are displayed as the lower dotted curve. The implied column density is $N({\rm Si}^+) = 1.9 \times 10^{16}$ cm^{-2} for the adopted oscillator strength $f = 4.25 \times 10^{-6}$ that is based on the measured lifetimes of Calamai et al. (1993).

The Ni II profile fitting was done for the $\lambda 1804$ line, which was observed with Echelle-B. The fit was verified for the $\lambda 1709$ feature, observed at lower resolution but higher S/N. The results were gratifyingly consistent, allowing us some confidence in the derived column densities.
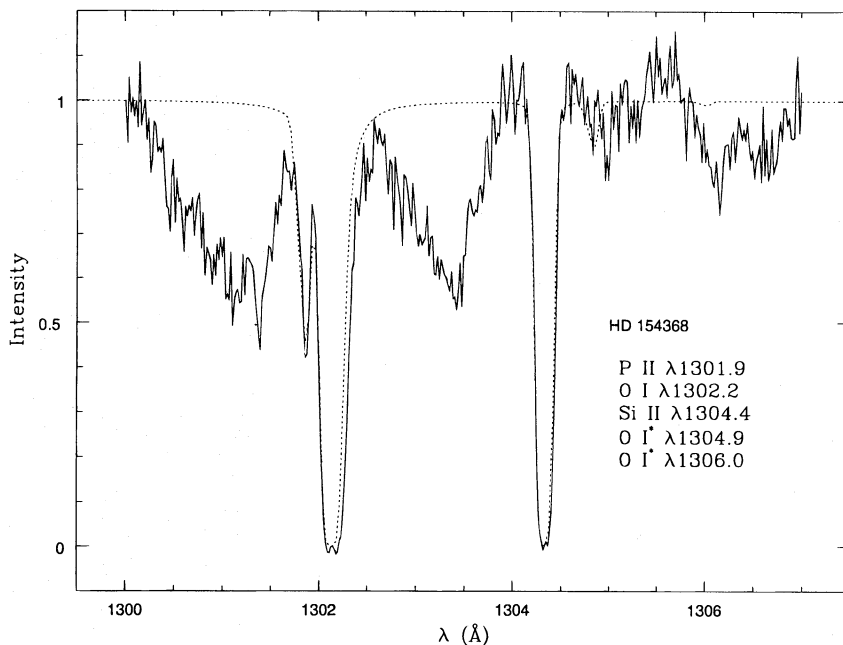

FIG. 6.—The spectrum in the vicinity of the saturated O I $\lambda 1302$ line is shown as the solid curve. The dotted curve is a simulated spectrum that includes the prominent lines of P II, O I, and Si II, plus examples of the weak O I features arising in the excited fine-structure levels. The Ca II velocity model has been employed, and the adopted column densities are 4.0×10^{14}, 1.2×10^{18}, 2.0×10^{16}, 2.0×10^{13}, and 1.6×10^{12} cm^{-2} for P$^+$, O($^3P_2$), Si$^+$, O($^3P_1$), and O($^3P_0$), respectively.
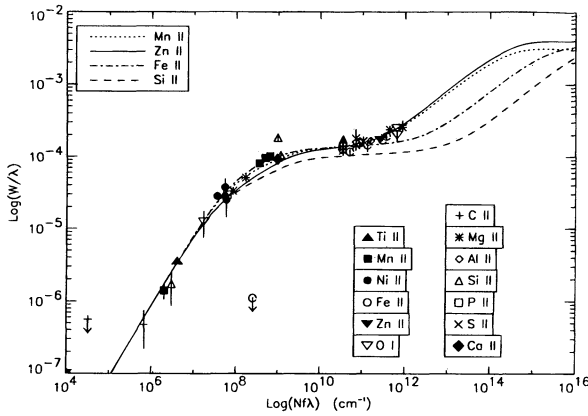
FIG. 8.—Curve of growth for ions. Seven component curves of growth were constructed for several species (indicated in legend at upper left) and then used to find column densities of a few species having only *IUE* data available. Results of the column density determinations are listed in Table 7.

The other species shown in Table 6 were fitted routinely, with no particular problems or inconsistencies, and they are not discussed further here.

6.3. *The IUE Data: Curve-of-Growth Analysis*

The spectra obtained with the *IUE* lack sufficient resolving power and S/N to justify profile fitting. Nevertheless, these data provide coverage of ions and lines not available in our *HST* data set, so it is useful to include them in the
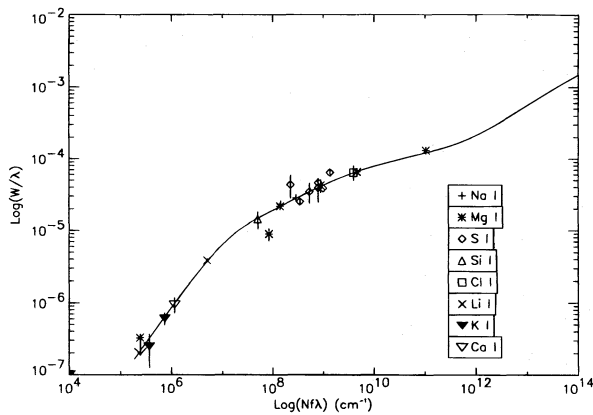
FIG. 9.—Curve of growth for neutrals. The solid line represents the seven component curve of growth based on the Na I profile. Other observed neutral atomic lines are indicated. This curve was used to derive column densities of species for which only one line was available or for which the data quality was insufficient to allow profile fitting.

TABLE 7

CURVE-OF-GROWTH COLUMN DENSITIES

Species	log N (cm^{-2})
Li I	11.18
Mg I	15.00
Al II	15.63
Si I	13.08
P II	14.60
Cl I	14.50
K I	12.50
Ca I	10.42[a]

[a] Gredel et al. 1993

analysis. The traditional method for deriving interstellar column densities from *IUE* data is to carry out a curve-of-growth analysis (e.g., Spitzer 1978; Morton 1975). Normally this is limited in accuracy by the a priori lack of knowledge of the *b*-values, and by the usual starting assumption that there is only a single cloud in the line of sight.

In this case, however, these obstacles can be surmounted by making use of information derived from the high-resolution ground-based and *HST* data. We have constructed theoretical curves of growth for several lines, based on the assumption that there are seven velocity components present, and adopting the velocity separation, relative column densities, and *b*-values for those components that were derived from the profile fitting analysis of the *HST* data. Thus, for these lines we have constructed realistic multicomponent curves of growth that represent the line of sight toward HD 154368. These curves can then be used to interpret the data on other species observed with the *IUE*.

To do this, some assumptions must be made which cannot be checked easily. For example, we assume that the species observed with the *IUE* share the same relative abundances among the seven cloud components as the species for which the curve of growth was constructed. Thus, when using the curve of growth derived from the Si II λ1808 line to analyze the Fe II lines observed with the *IUE*, we assume that Fe II has the same relative abundances among the seven components as Si II does. This assumption would surely fail for some species; for example, we would not expect the S I lines to follow the same distribution as Si II, both because S I is a minor ionization stage whereas Si II is the dominant stage, and because sulfur is usually little depleted while silicon is normally very depleted.

In order to address this issue, we constructed theoretical seven-component curves of growth for several different species for which we had line profile fits, and we compared the results to determine the effect of varying depletion patterns as a function of velocity. On the whole, we found good consistency among Zn II, Si II, Mn II, and Fe II (see Fig. 8), but there were substantial differences in the saturated portion (log $Nf\lambda \approx 10^8$–10^{12} cm^{-1}), and in the region in which the differing damping constants of the lines become important (log $Nf\lambda \geq 10^{12}$ cm^{-1}), but few lines are strong enough to lie in this region. The ions in general fit the curves representing Mn II and Zn II the best. Therefore, we used these curves in deriving column densities for new species.

For the neutrals we used only the Na I curve of growth (Fig. 9), which was computed for the D1 line, incorporating the hyperfine components. This provides a very good fit for species such as S I, for which we had a number of lines available and was therefore used to derive column densities of other neutrals. We note, however, that O I fits the curve of growth for first ions better than it does the curve for neutrals; this is not surprising, since oxygen is expected to be neutral throughout the H I gas.

The good fit of most ions to the seven-component curve of growth based on our line profile fit is useful for at least two reasons: (1) it helps to confirm and verify the consistency of our profile fits; and (2) it demonstrates that the multicomponent curves of growth should be useful for estimating column densities of additional species.

Having demonstrated that the multicomponent curves of growth yield a reasonable representation of the line of sight, we then used them to derive column densities for a few species for which we had no other means of obtaining

abundance information. The results for these species are presented in Table 7.

7. DEPLETIONS IN THE TWO MAIN COMPONENTS

We have used the results of the profile fitting and the curve-of-growth analyses to estimate the depletions of the elements from the gas phase for the line of sight toward HD 154368. We are able to derive the depletions separately for the total line of sight (i.e., for the sum of all the cloud components) and for the two components that contain most of the mass. The results for the minor components are not sufficiently reliable to justify depletion calculations.

For the integrated column densities, we were able to calculate depletions relative to hydrogen, the normal standard. We could not do so for the individual cloud components, however, because the hydrogen abundance could not be measured separately for individual clouds along the line of sight.

Cold molecular hydrogen is not directly observable with *HST* because the lines arising in its vibrational ground state ($v = 0$) all lie at wavelengths $\lambda < 1110$ Å, where GHRS is insensitive. Thus, in order to estimate the total hydrogen column density, we were forced to rely on empirical correlations between H_2 and other, observable, species. This is discussed in detail in Paper II, where it is shown that three different surrogates yield an estimated H_2 column density of $N(H_2) = 1.6 \times 10^{21}$ cm^{-2}, with a scatter of $\pm 20\%$. Combining this with our value of $N(H) = 1.0 \times 10^{21}$ cm^{-2} leads to a value for the total hydrogen column density of $N_H = N(H) + 2N(H_2) = 4.2 \times 10^{21}$ cm^{-2}.

Table 8 summarizes all the column densities and lists the depletions for the integrated line of sight, based on the value of N_H just described. The reference abundances listed there and used in calculating the depletions are based on solar photospheric abundances (Anders & Grevesse 1989; Grevesse et al. 1990, 1991). As pointed out by Sofia, Cardelli, & Savage (1994), the interpretation of the depletions of elements like carbon depends upon the adopted reference abundances. On the one hand, adoption of the solar carbon abundance as the standard implies generally significant carbon depletions, but on the other hand the carbon abundances in young stars (e.g., Gies & Lambert 1992), which

presumably represent the current composition of the interstellar medium, imply little or no carbon depletion. Snow & Witt (1995) have proposed a reduction of the cosmic carbon abundance, and it appears that other species may be similarly revised. For now, however, we adopt the solar values so that we may make comparative remarks pertaining to relative depletions in HD 154368 and other stars whose depletions were measured according to the same standard.

The depletion results are shown also in Figure 10. The overall depletions tend to be less in general than those found for less reddened lines of sight observed with *Copernicus* and the *IUE* (e.g., Morton 1974, 1975; Snow 1976, 1977; Joseph et al. 1986). This may appear surprising, in view of the fact that HD 154368 presents a more heavily obscured line of sight than was accessible to these earlier instruments. One might suspect that some of the earlier derivations of depletions were overestimated due to incorrect column densities, because at the lower spectral resolutions of instruments such as *Copernicus* and *IUE* it is easier to underestimate column densities by ignoring unresolved cloud components. But some of the results we compare our data with, such as those on ζ Oph (also shown
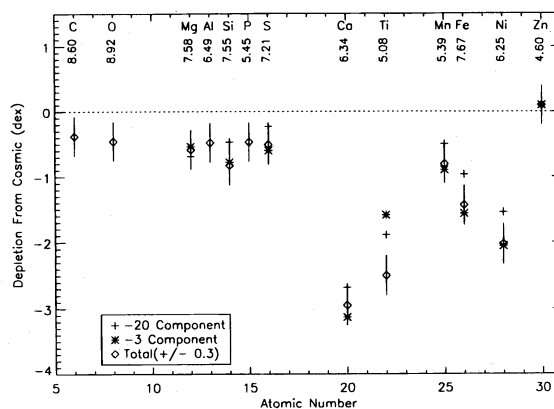

FIG. 10.—Depletion pattern for HD 154368. Symbols as indicated in the key represent depletions for the velocity components at -20.95 km s^{-1} and -3.26 km s^{-1} as well as for the total integrated line of sight (see Table 8).

TABLE 8
COLUMN DENSITIES AND DEPLETIONS[a]

| SPECIES | REFERENCE ABUNDANCE[b] | COLUMN DENSITIES | | | DEPLETION | | | |
		$V_{Helio} = -20$	$V_{Helio} = -3$	Total	$V_{Helio} = -20$	$V_{Helio} = -3$	Total	ζ Oph[c]
H I, H_2	12.00	[3.3E(20)]	[4.0E(21)]	4.2E(21)	...	...	...	...
C I, II	8.60	...	...	7.0E(17)	...	...	-0.38	-0.48
O I................	8.92	...	...	1.2E(18)	...	...	-0.46	-0.46
Mg I, Mg II	7.58	2.0E(15)	3.5E(16)	4.1E(16)	-0.80	-0.64	-0.59	-0.92
Al I, Al II	6.49	...	...	4.3E(15)	...	...	-0.48	-2.60
Si I, Si II	7.55	3.1E(15)	1.9E(16)	2.2E(16)	-0.58	-0.87	-0.83	-1.72
P II	5.45	...	...	4.0E(14)	...	...	-0.47	-1.11
S I, S II	7.21	2.5E(15)	1.3E(16)	2.1E(16)	-0.33	-0.70	-0.51	-0.31
Ca I, Ca II	6.34	9.7E(11)	2.7E(12)	5.4E(12)	-2.87	-3.51	-3.21	-2.57
Ti I, Ti II	5.08	4.0E(11)	1.0E(12)	1.6E(12)	-2.00	-2.68	-2.50	-2.72
Mn I, Mn II	5.39	2.0E(13)	1.0E(14)	1.6E(14)	-0.61	-0.99	-0.81	-1.23
Fe I, Fe II	7.67	1.3E(15)	4.0E(15)	7.2E(15)	-1.07	-1.67	-1.44	-2.12
Ni II	6.25	1.3E(13)	5.0E(13)	7.0E(13)	-1.65	-2.15	-2.03	-2.24
Zn II	4.60	1.3E(13)	1.6E(14)	2.1E(14)	[0.0]	[0.0]	$+0.10$	-0.44

[a] Column densities are in units of cm^{-2}; depletions are logarithmic with respect to the listed reference abundances.

[b] Reference abundances are logarithmic relative to hydrogen by number of nuclei, on a scale in which [H] = 12.0; see text for references.

[c] From Cardelli et al. 1993 for carbon and oxygen; from Lepp et al. 1988 for other species.

in Table 8), are based on highly accurate GHRS *HST* data and probably do not suffer from this problem. We conclude that the lower depletions toward HD 154368 are real. The possible interpretation of this result is discussed below.

Sulfur appears to be an exception to the general trend, being more depleted in HD 154368 than in ζ Oph. It is not clear how significant this result is, however; the allowed range in the S depletion, ±0.3 dex, permits agreement with the ζ Oph depletion.

Because we do not know the distribution of hydrogen (H or H_2) among the various velocity components, we must use another element as a reference standard for analyzing the variation of relative abundances. Preferably this element should be undepleted in the interstellar medium and should exist predominantly in one stage of ionization over a range of conditions. Our analysis indicates that the overall sulfur/hydrogen ratio is significantly less than solar, suggestive of depletion. Zinc has been proposed as a widely observed, undepleted element in the diffuse interstellar medium (e.g., York & Jura 1982); however, two recent studies show that its abundance in the gas phase is approximately 65% of the solar abundance in thin clouds of low molecular fraction (Sembach et al. 1995; Roth & Blades 1995). Moreover, these investigations reveal a tendency of the apparent Zn/H ratio to correlate with $N(H)$ or with molecular fraction $[f(H_2) = 2n(H_2)/N_H]$, which argues that the subsolar abundance is an effect of depletion. Even so, we will use zinc (as represented by Zn II absorption) for scaling the abundances of other elements in order to see if there are large variations from one component to another.

The derived total abundance of zinc, which is based on high-quality Echelle-B data, suggests that this element is depleted by no more than −0.2 dex in the line of sight toward HD 154368. The relative abundances and depletions in the two main velocity components are displayed in Table 8. The adopted hydrogen column densities for these components assume undepleted zinc (i.e., H/Zn = 2.5 × 10^7 as in the solar photosphere): these values are displayed in brackets in the table.

It is not feasible to derive meaningful estimates of depletion for the minor velocity components because these components contain in aggregate less than 1% of the total column density. Thus, small errors in the profile fits for these components would amount to large relative uncertainties in the column densities.

The depletions for the two main components, at −3.26 and −20.95 km s^{-1}, are quite similar; i.e., both clouds show substantial depletions (but both are lower than the values for ζ Oph). This line of sight, therefore, appears to contain two major diffuse clouds, in contrast with the situation found in many previous studies in which there was one main cloud (usually at low LSR velocity) and one or more subordinate clouds which often showed lower depletions. The common interpretation of these situations was that the secondary component(s) represented shocked gas which may be physically associated with the main low-velocity cloud; the shocked gas (high-velocity component) usually showed smaller depletions (e.g., Snow & Meyers 1979). But toward HD 154368 both the main components have depletions characteristic of "normal" low-velocity clouds and therefore are likely to be distinct clouds lying along the line of sight. It would be interesting to analyze the minor components to see whether they follow the normal pattern of high-velocity shocked gas having little or no depletion.

The depletions relative to zinc for the two main clouds are depicted graphically in Figure 10. The pattern of relative depletions, from element to element, is reasonably constant. In general the depletions in the −3.26 km s^{-1} cloud are larger by about 0.35–0.45 dex than in the −20.95 km s^{-1} component, although for iron the difference is greater (0.60 dex). The only exception among the elements included in our study is magnesium, which has a greater depletion in the −20.95 km s^{-1} component by 0.16 dex, a small effect, which is still significant in a relative sense.

As discussed in § 2, the densest gas in the line of sight toward HD 154368 is contained within the −3.26 km s^{-1} component. This component is where the molecular lines (both optical absorption and millimeter-wave emission) arise, and as discussed below, it is also the home of the neutral atomic lines. Thus, the enhanced depletions in this cloud, as opposed to the less dense −20.95 km s^{-1} component, are consistent with the idea that depletions are a function of cloud density (e.g., Snow & Jenkins 1980; Joseph et al. 1986). This conclusion may be interpreted as indicating that some portion of the depletions is density dependent either because the deposition of atomic species onto the dust grains occurs within the clouds and is thus more efficient in denser regions, or because processes that remove atomic species from grain surfaces occur more readily in less dense regions (e.g., see discussion in Savage & Bohlin 1979). It is possible that the lesser depletions in less dense components is related to sputtering of atoms off of grains due to shocks, which can penetrate more deeply into less dense regions (sputtering and depletions were originally discussed by Barlow & Silk 1978).

In summarizing our depletion results, we emphasize the following: (1) the overall depletions are lower than inferred previously for moderately reddened diffuse-cloud lines of sight; (2) it appears that zinc is almost undepleted and can be used as a standard for comparison, to analyze relative abundances in individual cloud components; and (3) in this particular line of sight, unlike most of those previously analyzed, there appear to be two distinct moderately dense diffuse clouds, each having significant depletions, but one (the lower-velocity component) having more depletion than the other, indicating that at some level the depletion process is density dependent.

8. NEUTRAL ATOMS

The column densities of neutral atomic species observed with *HST* were derived in the same fashion as were the abundances of ions, described earlier. For many species, profile fitting was employed; for some, curve-of-growth analysis was also carried out. The profile fits for neutrals were included in Table 6, and the equivalent widths were included in Table 5. The final column densities are shown in Table 9. The two best-determined neutral species (other than Na I and Ca I) were C I and S I, both of which have many lines in the grating G160M wavelength region, with a wide range of *f*-values. For C I, excited fine-structure levels of the ground term are populated so that each transition appears as a multiplet, barely resolved with grating G160M. Thus, profile fitting was essential in the derivation of C I column densities; one side benefit was the determination of the relative populations in the fine-structure states, which serve as diagnostics of cloud physical parameters (see Paper II). For S I, the lines are well separated and do not show fine-structure components, and it proved feasible to

TABLE 9

Column Densities of Neutral Atoms

Species	N (cm^{-2})	Source
Li I	1.30E(11)	ESO, weak-line limit; curve of growth
C I........	1.67E(16)	Profile fit, numerous multiplets, G160M grating
O I........	1.20E(18)	Profile fit, 1355 Å line, G160M grating
Na I	4.28E(14)	Profile fit, UHRF data
Mg I......	3.09E(14)	Profile fit, Echelle-B data; curve of growth
Al I	≤4.3E(11)	Echelle-B data
Si I........	1.20E(13)	curve of growth
S I	5.69E(13)	Profile fit, Echelle-B; curve of growth
Cl I	2.51E(15)	curve of growth
K I........	2.50E(12)	ESO data, weak-line limit
Ca I	2.6E(10)	Gredel et al. 1993
Ti I	≤1.2E(11)	ESO data, weak-line limit
V I........	≤1.2E(11)	ESO data, weak-line limit
Cr I	≤1.1E(11)	ESO data, weak-line limit
Mn I......	≤1.1E(11)	ESO data, weak-line limit
Fe I	7.70E(11)	ESO data, weak-line limit
Ni I	1.07E(11)	Profile fit, Echelle-B data

augment the profile fitting with a curve-of-growth analysis, using the velocity structure for the line of sight that was deduced from the Na I profile fit, as described earlier.

8.1. *Ionization Balance*

The ratio of neutral atomic column densities to those of first ions of the same elements, together with the standard equations of ionization equilibrium (e.g., Spitzer 1975), can provide information on the local radiation field and the electron density. Use of this technique necessarily invokes certain assumptions which are probably oversimplified. For example, normally it is assumed that the neutrals and ions are located in the same region, whereas in fact they may arise in different physical locations along the line of sight, rendering the comparison of the two in deducing cloud physical conditions less meaningful. This problem plagued ionization balance studies done using *Copernicus* data, for example (e.g., Morton 1975; Snow 1976). The species in the present study that have been analyzed using profile fits for Echelle-B data, however, can provide more accurate results, since we can compare neutrals and ions for the same velocity component.

We can make rough estimates of the electron density under the following assumptions: (1) that the neutral and first ion are distributed identically along the line of sight; (2) that the rates of photoionization and radiative recombination are constant throughout; and (3) that no other processes affect the ionization balance. In this case, the column-averaged electron density is

$$\langle n_e \rangle \approx \frac{N_{\rm atom}}{N_{\rm ion}} \frac{\Gamma}{\alpha} \; {\rm cm}^{-3} \; ,$$

where $N_{\rm atom}$ and $N_{\rm ion}$ are the column densities of the neutral and corresponding first ion, respectively, Γ is the rate of photoionization of the neutral in units of s^{-1}, and α is the rate coefficient of radiative recombination in units of cm^3 s^{-1}. We have adopted the photoionization rates tabulated by van Dishoeck (1988), which are based on the mean background starlight spectrum of Draine (1978). The recombination coefficients are from Péquignot & Aldrovandi (1986) and Weisheit (1973).

Table 10 lists the derived values for the electron density n_e, for the species for which we have sufficient information on the column densities if the neutral atom and the first ion. These values for n_e refer to the integrated line of sight, since we have component information on neutral atoms in only a very few cases. Where we do have such information (primarily for carbon and sulfur), there was no significant difference between the values of n_e derived for the -20.95 and -3.26 km s^{-1} components.

TABLE 10

Ionization Balance and the Electron Density

Element	Ionization Potential (eV)	Γ^a (s^{-1})	α^b (cm^3 s^{-1})	log $N_{\rm atom}$ (cm^{-2})	log $N_{\rm ion}$ (cm^{-2})	$N_{\rm atom}/N_{\rm ion}$	$\langle n_e \rangle$ (cm^{-3})
C........	11.260	3.0E(−10)	1.8E(−11)	16.22	17.85	0.0234	0.39
Mg......	7.646	7.9E(−11)	1.3E(−11)	14.49	16.61	0.00759	0.046
Al	5.986	4.7E(−9)	3.1E(−11)	≤11.64	15.63	≤0.0001	≤0.016
Si........	8.151	3.1E(−9)	1.8E(−11)	13.08	16.34	0.00055	0.095
S	10.360	5.9E(−10)	2.1E(−11)	13.76	16.32	0.00275	0.077
Ca	6.113	3.4E(−10)	1.5E(−11)	10.42	12.73	0.00490	0.11
Ti	6.821	2.3E(−10)	1.2E(−11)	≤11.07	12.09	≤0.0955	≤1.8
Mn......	7.434	3.3E(−10)	1.2E(−11)	≤11.09	14.20	≤0.00078	≤0.006
Fe.......	7.870	2.8E(−10)	1.2E(−11)	11.89	15.86	0.00011	0.0025
Ni	7.635	9.8E(−10)	1.3E(−11)	11.03	13.84	0.00155	0.012

[a] Values of the photoionization rate Γ are for the average interstellar radiation field of Draine 1978 and have been tabulated by van Dishoeck 1988.

[b] Values of the recombination coefficient α are taken from Péquignot & Aldrovandi 1986 except for carbon (Weisheit 1973) and have been evaluated at $T = 30$ K.

TABLE 11
RELATIVE DEPLETIONS IN THE NEUTRAL CLOUD CORE

Element	$N_{atom}/N_{S\,I}$	$N_{ion}/N_{S\,II}$	$\zeta_{neutral}$	ζ_{total}
C	293	33.3	+1.07	−0.11
Mg	5.43	1.95	−0.37	−0.08
Al	≤0.0076	0.25	≤−1.40	+0.03
Si	0.21	1.05	−1.02	−0.32
Ca	0.00046	0.00026	−2.45	−2.70
Ti	≤0.0021	0.000076	≤−0.55	−1.99
Mn	≤0.0019	0.0076	≤−0.90	−0.30
Fe	0.0135	0.34	−2.33	−0.93

A value $\langle n_e \rangle \approx 0.05$–$0.1$ cm^{-3} is derived from the ionization of Mg, Si, S, and Ca, consistent with the value of $n_e \approx 0.04$–0.15 cm^{-3} determined from the excess excitation of CN in the main component by Black & van Dishoeck (1991). The ionization of Al, Mn, Fe, and Ni suggests much lower electron densities. The ionization balance of carbon is known to be affected by shielding of the C photoionization by H_2 and by chemical processes that transform carbon into CO and other molecules; therefore, this simple ionization analysis is not expected to yield a useful result for carbon. As discussed by Lepp et al. (1988), both large molecules (e.g., PAHs) and the effects of stratification will cause the true ionization balance to differ from this very simple representation of $\langle n_e \rangle$. It is also possible that the discrepancies in ionization estimates are caused by the varying depletions of the different elements within the neutral atomic zone of a stratified cloud (i.e., the cloud core). For example, if the depletions of aluminum, manganese, and iron are enhanced in the cloud core, then the column densities of the neutral atoms of these elements would be decreased relative to the column densities of the first ions, and lower electron densities would be inferred. Similarly, the high value for n_e derived from the sulfur ionization ratio could be explained by a relatively low depletion of sulfur in the cloud core. This would be particularly interesting, since it appears that there is some depletion of sulfur over the integrated line of sight.

In any case, most of the free electrons come from ionization of carbon, so that the column-averaged ionization fraction, $\langle n_e/n_H \rangle \geq N(C^+)/N_H \approx 1.7 \times 10^{-4}$, is in harmony with a total density,

$$n_H \approx \frac{\langle n_e \rangle}{\langle n_e/n_H \rangle} \leq 600 \left(\frac{\langle n_e \rangle}{0.1 \text{ cm}^{-3}} \right) \text{cm}^{-3} \, ,$$

in the densest component. For comparison, the C_2 excitation analysis by van Dishoeck & de Zeeuw (1984) gives $n_H \approx 350$ cm^{-3} for the -3 km s^{-1} component. The column-averaged value of n_H, derived from the ratio of the total hydrogen column density and the estimated distance to the star, is of course much smaller: $\langle n_H \rangle \approx 1.7$ cm^{-3}.

Further details of the volume density in the clouds seen toward HD 154368 will be presented in Paper II, which discusses detailed models of the cloud chemistry and physical conditions.

8.2. Depletions in the Cloud Core Derived from Neutral Species

It is possible, using relative column densities of neutral atomic species, to derive *relative* depletions in the cloud core, the region in which the neutral species arise. This idea was exploited by Snow (1984), who summarized data on neutral atomic species in several lines of sight and com-

pared depletions in the cloud cores with integrated line-of-sight depletions based on the dominant first ions. In general, the survey of Snow revealed cloud core depletions that were quite consistent with the integrated depletions, indicating that little enhancement of depletion was taking place in the relatively dense regions in which the neutral species reside. The one exception to this was ζ Oph, which showed enhanced depletions in the cloud core.

The method is based on a division of the ionization balance equation for two elements, A and B, which results in

$$\frac{n_A^+}{n_B^+} = \frac{n_A^0}{n_B^0} \frac{(\Gamma/\alpha)_A}{(\Gamma/\alpha)_B} \, ,$$

where the n^+ represent the first ions, n^0 represent the neutral atoms, and Γ and α are the photoionization rate and the radiative recombination rate coefficient, respectively.

Substitution of the observed column density ratio N_A^0/N_B^0 for the corresponding volume density ratio yields a value for the ratio of the first ions in the cloud core, which in turn can be used to estimate relative depletions, since even in the cloud core, the first ions are dominant.

Table 11 presents the results of this calculation for the species for which we had sufficient data to carry out the analysis. In these results, sulfur has been used as the reference element, on the assumption that it is relatively little depleted. Therefore, the depletions listed in Table 11 for the cloud core (i.e., the $\zeta_{neutral}$ values) actually represent depletions relative to sulfur, not hydrogen.

For carbon, magnesium, and calcium, the inferred depletions are greater than or comparable to those for the integrated line of sight. But for aluminum, silicon, manganese, and iron, significant enhancements to the depletion are inferred. This appears to indicate that these elements suffer enhanced depletions in the cloud core, which suggests that accretion of these species onto dust grains is taking place there. There have been previous indications that both manganese and iron undergo enhanced depletions in the cores of diffuse clouds (Joseph et al. 1986; Joseph 1988; Joseph, Snow, & Seab 1989), so our results for HD 154368 appear to support a trend already suspected.

The selective depletion of certain elements in dense regions potentially may provide useful information on the general depletion process and on the details of grain surface chemistry and adsorption. It is found in general that the relative depletions of the elements (the so-called depletion pattern) is invariant in diffuse clouds; only in dense regions such as neutral cloud cores do we begin to see clear signs of selective depletions. It would, of course, be very interesting to push this kind of study into even denser regions such as true molecular clouds. Studies based on millimeter-wave observations of molecules suggest very strongly enhanced depletions of sulfur do occur in denser photon-dominated regions such as the reflection nebula IC 63 (Jansen, van Dishoeck, & Black 1994).

9. SUMMARY AND DISCUSSION

Our analysis of the atomic column densities and depletions toward HD 154368 has revealed the following:

1. *General line of sight.*—HD 154368 is located about 800 pc away and lies far beyond the main observed interstellar clouds, which are at ~ 125 pc and probably associated with the Sco-Cen Loop I supernova remnant. Thus, the star has

little direct effect on the physics and chemistry of the observed gas, which may therefore be treated as isolated interstellar clouds.

2. *Cloud structure.*—The line of sight contains two significant diffuse clouds, at heliocentric velocities of -20.95 and -3.26 km s^{-1}. Together these clouds contain more than 80% of the total material in the line of sight, based on the distribution of Zn II absorption, with about 76% in the -3.26 km s^{-1} component.

3. *Ultraviolet extinction.*—The *IUE* data show that the extinction curve for HD 154368 is close to the average curve. It can be well represented by the Fitzpatrick & Massa parameterization, with only a slight deviation of the sort normally found in dark clouds. Thus, the extinction curve shows no evidence of grain-modification processes that might be expected in a dense molecular cloud.

4. *Velocity structure.*—The Na I D1 absorption line, observed at very high spectral resolution ($R \approx 10^6$), is best fit by a computed profile containing seven velocity components, although as noted above, most of the mass arises in the two main clouds. The other five components are required in order to find satisfactory fits to the line profiles, but their contribution to the total column density is small, and the uncertainties in their relative compositions make it difficult to derive much useful information about their physical and chemical states.

5. *Profile fits to the HST data.*—Several lines of both neutral atomic species and ions observed with the GHRS were well fitted by assuming the velocity model derived from the Na I analysis and from a similar model distribution based on a published Ca II profile (Crawford 1992). This permitted detailed analyses of the composition and depletions in the main clouds.

6. *Depletions in the main clouds.*—Both the principal clouds show depletion patterns typical of diffuse clouds, with total depletions not much larger than in ordinary lines of sight of lower total column density. One contributing factor to this apparent contrast between the HD 154368 line of sight and others (such as ζ Oph) that have greater measured depletions may be the neglect of hidden components in lines of sight analyzed with data inferior to that from the GHRS. However, we conclude that this kind of oversight in previous analyses cannot explain the contrast fully. Thus, we infer that the HD 154368 line of sight contains two substantial, but diffuse, clouds of significant physical extent with no true molecular cloud core. The -3.26 km s^{-1} component shows greater depletions than the -20.95 km s^{-1} cloud and also contains the bulk of the molecular material, so it is closer to representing a molecular cloud core, but even this cloud shows substantially lesser molecular processing and gas-dust interaction than a true molecular cloud.

7. *Curve of growth.*—A semiempirical, multicomponent curve of growth, based on the inferred velocity structure and relative component densities, proved to be an adequate representation of the line of sight, providing a consistency check on the line profile analyses, and also allowing the derivation of column densities for species for which we lack high-resolution profiles.

8. *Ionization balance and the electron density.*—Compositions of derived column densities for neutral atoms and first ions of several elements provide estimates of the value of the electron density. For several species consistent values were found (average $n_e \approx 0.1$ cm^{-3}), in harmony with a total density in the cloud core region of $n_H \leq 600$ cm^{-3}. Some elements (specifically manganese and iron) yielded much smaller values of n_e, implying that these elements may be much more depleted in the cloud core, relative to the other species.

9. *Depletions inferred from neutral atoms.*—Comparison of the column densities of neutral atomic species yields estimated relative column densities of the dominant first ions in the cloud core. From these, relative depletions in the cloud core were inferred, which showed that certain species (notably, manganese and iron) appear to suffer enhanced depletions.

From these results, we suggest that this "translucent" line of sight resembles thinner diffuse clouds. One of the components, at a heliocentric velocity of -3.26 km s^{-1}, contains most of the (substantial) molecular column density in the line of sight, and thus it is closer to representing a molecular cloud. But the lower depletions (and lower volume density; see Paper II) indicate that the large molecular column densities must arise over a long path length through the cloud, rather than from a concentrated region of high density.

The presence of two significant diffuse clouds in a single line of sight is unusual; previous analyses of abundances and depletions in lines of sight having multiple components have usually shown that all but the main cloud have relatively low depletions. These secondary clouds are usually assumed to have been accelerated by shocks that have destroyed dust grains, thus reducing the depletions (e.g., Shull 1977; Snow & Meyers 1979).

It is also interesting that the two main clouds in the HD 154368 line of sight are both thought to be associated with an expanding supernova remnant, the Loop I remnant in the Sco-Cen complex (but see discussion of alternative interpretations in § 1.2). Thus, one might expect to find reduced depletions, if some grain destruction has occurred in the acceleration of these clouds. If so, the destruction was very limited in extent, since significant depletions are still found. The cloud velocities, which are rather low as compared with many observed clouds that have been accelerated by supernova shocks, may be consistent with little or no grain destruction. It has been suggested elsewhere (Meyers et al. 1985) that low-velocity shocks may actually enhance depletions, but we see little evidence of that in this case.

The ultraviolet extinction curve for HD 154368, which we have shown to be close to the "average" curve for diffuse clouds, is also consistent with the general picture that the clouds in this line of sight do not represent true molecular clouds. As we have seen, the extinction curve has at most only a small contribution from the kind of dust observed in dark clouds.

A detailed analysis of the physical and chemical processes within the main cloud at -3 km s^{-1} toward HD 154368 will be presented in Paper II. This analysis lends further support to the general picture to the clouds seen in this line of sight represent extended regions of moderate-density gas, rather than containing any significant molecular cloud cores.

TABLE 12

RECOMMENDED OSCILLATOR STRENGTHS AND UPPER STATE INVERSE LIFETIMES

Transition (l–u)	λ_{vac} (Å)	f	ΣA (s^{-1})	Reference
$3s^2 3p\,^2P^o$–$3s3p^2\,^4P$:				
$J = 3/2$–$5/2$	2335.321	3.017E(-6)	2.460E($+3$)	1
$J = 3/2$–$3/2$	2344.920	1.006E(-6)	1.230E($+3$)	1
$J = 1/2$–$3/2$	2329.231	1.627E(-8)	1.230E($+3$)	1
$J = 3/2$–$1/2$	2350.892	1.827E(-6)	9.610E($+3$)	1
$J = 1/2$–$1/2$	2335.123	4.251E(-6)	9.610E($+3$)	1
$3s^2 3p\,^2P^o$–$3s3p^2\,^2D$	1814	1.87E(-3)		1
$J = 1/2$–$3/2$	1808.0126	2.08E(-3)	2.38E($+6$)	2
$J = 3/2$–$5/2$	1816.9285	1.65E(-3)	2.24E($+6$)	2
$J = 3/2$–$3/2$	1817.4512	1.28E(-4)	2.38E($+6$)	2
$3s^2 3p\,^2P^o$–$3s^2 4s\,^2S$	1531	1.30E(-1)	1.106E($+9$)	3
$3s^2 3p\,^2P^o$–$3s3p^2\,^2S$	1308	8.82E(-2)	1.033E($+9$)	3
$3s^2 3p\,^2P^o$–$3s^2 3d\,^2D$	1263	1.164	2.915E($+9$)	3
$3s^2 3p\,^2P^o$–$3s3p^2\,^2P$	1194	8.71E(-1)	4.065E($+9$)	3

REFERENCES.—(1) Calamai et al. 1993; (2) Bergeson & Lawler 1993; (3) Hibbert et al. 1992

APPENDIX A

Si II OSCILLATOR STRENGTHS

The oscillator strengths recommended by Morton (1991a, b) for several multiplets of Si II are almost certainly incorrect. Morton adopted the empirical, astronomical oscillator strengths of Shull, Snow, & York (1981), which were based upon spectra of relatively coarse resolution. Dufton et al. (1983) had argued previously that these oscillator strengths could not be correct. More recently, there have been independent experimental (Bergeson & Lawler 1993) and theoretical (Dufton et al. 1992) determinations of the oscillator strengths in the weak multiplet at 1808 Å, which had previously been the most uncertain, and in many ways the most important, of the Si II f-values. The agreement between theory and experiment is excellent, within the estimated uncertainties of either result. This provides further impetus to prefer the best theoretical calculations for the stronger transitions, which are even less troubled by effects of cancellation and mixing in the numerical wave functions. The theoretical results used by Dufton et al. (1992) are described in detail by Hibbert, Ojha, & Stafford (1992). We believe that these should be preferred for all resonance lines of Si II (but with the measurements of Bergeson & Lawler for the λ1808 multiplet) and that Morton's recommendations should be ignored.

There is also an accurate laboratory measurement for the intersystem transition Si II]$^4P \to {}^2P^o$ at 2335 Å (Calamai et al. 1993).

The recommended oscillator strengths and upper-state inverse lifetimes are listed in Table 12.

Note that oscillator strengths are listed for the individual lines in the first two multiplets, where the line strengths differ strongly from those expected in LS coupling. For the remaining transitions, only multiplet values are listed. In those cases, f-values for individual lines can be scaled relative to the line strengths listed by Morton (1991a, b).

REFERENCES

Anders, E., & Grevesse, N. 1989, Geochim. Cosmochim. Acta, 53, 197
Barlow, M. J., Crawford, I. A., Diego, F., Dryburgh, M., Fish, A. C., Howarth, I. D., Spyromilio, J., & Walker, D. D. 1995, MNRAS, 272, 333
Barlow, M. J., & Silk, J. I. 1978, ApJ, 211, L83
Bergeson, S. D., & Lawler, J. E. 1993, ApJ, 414, L137
Black, J. H. 1985, in Molecular Astrophysics: State of the Art and Future Directions, ed. G. H. F. Diercksen, W. F. Huebner, & P. W. Langhoff (Dordrecht: Reidel), 215
Black, J. H., & van Dishoeck, E. F. 1991, ApJ, 369, L9
Blades, J. C. 1978, MNRAS, 185, 451
Blades, J. C., & Bennewith, P. D. 1973, MNRAS, 161, 213
Boggess, A., et al. 1978, Nature, 275, 372

Bohlin, R. C. 1975, ApJ, 200, 402
Bruhweiler, F. C., Gull, T. R., Kafatos, M., & Sofia, S. 1980, ApJ, 238, L27
Calamai, A. G., Smith, P. L., & Bergeson, S. D. 1993, ApJ, 415, L59
Cardelli, J. A., & Clayton, G. C. 1991, AJ, 101, 1021
Cardelli, J. A., Clayton, G. C., & Mathis, J. S. 1989, ApJ, 345, 245 (CCM)
Cardelli, J. A., Ebbets, D. C., & Savage, B. D. 1990, ApJ, 365, 789
———. 1993, ApJ, 413, 401
Cardelli, J. A., Sembach, K. R., & Mathis, J. S. 1992, AJ, 104, 1916
Cardelli, J. A., Sofia, U. J., Savage, B. D., Keenan, F. P., & Dufton, P. L. 1994, ApJ, 420, L29
Crawford, I. A. 1992, MNRAS, 259, 47
Crawford, I. A., Barlow, M. J., & Blades, J. C. 1989, ApJ, 336, 212

Crawford, I. A., Barlow, M. J., Diego, F., & Spyromilio, J. 1994, MNRAS, 266, 903
Crutcher, R. M. 1982, ApJ, 254, 82
———. 1985, ApJ, 288, 604
Crutcher, R. M., & Lien, D. J. 1984, in IAU Colloq. 81, The Local Interstellar Medium, ed. Y. Kondo, F. C. Bruhweiler, & B. D. Savage (NASA CP-2345), 117
Dame, T. M., et al. 1987, ApJ, 322, 706
de Gues, J., de Zeeuw, P. T., & Lub, J. 1989, A&A, 216, 44
Diego, F., et al. 1995, MNRAS, 272, 323
Draine, B. T. 1978, ApJS, 36, 595
Dufton, P. L., Hibbert, A., Kingston, A. E., & Tully, J. A. 1983, MNRAS, 202, 145
Dufton, P. L., Keenan, F. P., Hibbert, A. E., Ojha, P. C., & Stafford, R. P. 1992, ApJ, 387, 414
Fang, Z., Kwong, V. H. S., Wang, J., & Parkinson, W. H. 1993, Phys. Rev. A, 48, 1114
Fitzpatrick, E. L., & Massa, D. 1986, ApJ, 307, 286
———. 1988, ApJ, 328, 734
———. 1990, ApJS, 72, 163
Garrison, R. F., Hiltner, W. A., & Schild, R. E. 1977, ApJ, 35, 111
Gies, D. R., & Lambert, D. L. 1992, ApJ, 387, 673
Gredel, R., van Dishoeck, E. F., & Black, J. H. 1991, A&A, 251, 625
Gredel, R., van Dishoeck, E. F., & Black, J. H. 1993, A&A, 269, 477
———. 1994, A&A, 285, 300
Grevesse, N., Lambert, D. L., Sauval, A. J., van Dishoeck, E. F., Farmer, C. B., & Norton, R. H. 1990, A&A, 232, 225
———. 1991, A&A, 242, 488
Jansen, D. J., van Dishoeck, E. F., & Black, J. H. 1994, A&A, 282, 605
Hibbert, A., Ojha, P. C., & Stafford, R. P. 1992, J. Phys. B., 25, 4153
Johnson, H. L. 1966, ARA&A, 4, 193
Joseph, C. L. 1988, ApJ, 335, 157
Joseph, C. L., Snow, T. P., Jr., & Seab, C. G. 1989, ApJ, 340, 314
Joseph, C. L., Snow, T. P., Jr., Seab, C. G., & Crutcher, R. M. 1986, ApJ, 309, 771
Lennon, D. J., Dufton, P. L., Hibbert, A., & Kingston, A. E. 1985, ApJ, 294, 200
Lepp, S., Dalgarno, A., van Dishoeck, E. F., & Black, J. H. 1988, ApJ, 329, 418
Mathis, J. S., & Cardelli, J. A. 1992, ApJ, 398, 610
Meyers, K. A., Snow, T. P., Federman, S. R., & Breger, M. 1985, ApJ, 288, 148

Morton, D. C. 1974, ApJ, 193, L35
———. 1975, ApJ, 197, 85
———. 1991a, ApJS, 77, 119
———. 1991b, ApJS, 81, 883
Palazzi, E., Mandolesi, N., Crane, P., Kutner, M. L., Blades, J. C., & Hegyi, D. J. 1990, ApJ, 357, 14
Péquignot, E., & Aldrovandi, S. M. V. 1986, A&A, 161, 169
Riegel, K. W., & Crutcher, R. M. 1972, A&A, 18, 55
Roth, K. C., & Blades, J. C. 1995, ApJ, 445, L95
Roth, K. C., & Meyer, D. M. 1995, ApJ, 441, 129
Savage, B. D., & Bohlin, R. C. 1979, ApJ, 229, 136
Savage, B. D., & Mathis, J. S. 1979, ARA&A, 17, 73
Schild, R. E., Garrison, R. F., & Hiltner, W. A. 1983, ApJS, 51, 321
Seaton, M. J. 1979, MNRAS, 187, 73
Sembach, K. R., Steidel, C. C., Macke, R., & Meyer, D. M. 1995, ApJ, 445, L27
Shull, J. M. 1977, ApJ, 215, 805
Shull, J. M., Snow, T. P., & York, D. G. 1981, ApJ, 246, 549
Snow, T. P. 1976, ApJ, 204, 759
———. 1977, ApJ, 216, 724
———. 1984, ApJ, 287, 238
———. 1996, in preparation
Snow, T. P., & Jenkins, E. B. 1980, ApJ, 241, 161
Snow, T. P., Jr., & Meyers, K. A. 1979, ApJ, 229, 545
Snow, T. P., & Witt, A. N. 1995, Science, 270, 1455
Sofia, U. J., Cardelli, J. A., & Savage, B. D. 1994, ApJ, 430, 650
Spitzer, L. 1978, Physical Processes in the Interstellar Medium (New York: Wiley)
Spitzer, L., Jr., & Routly, P. M. 1952, ApJ, 115, 227
van Dishoeck, E. F. 1988, in Rate Coefficients in Astrochemistry, ed. T. J. Millar & D. A. Williams (Dordrecht: Kluwer), 49
van Dishoeck, E. F., & Black, J. H. 1988a, in Rate Coefficients in Astrochemistry, ed. T. J. Millar & D. A. Williams (Dordrecht: Kluwer), 209
———. 1988b, ApJ, 334, 771
———. 1989, ApJ, 340, 273
van Dishoeck, E. F., Black, J. H., Phillips, T. G., & Gredel, R. 1991, ApJ, 366, 141
van Dishoeck, E. F., & de Zeeuw, T. 1984, MNRAS, 206, 383
Vidal-Madjar, A., Laurent, C., Bonnet, R. M., & York, D. G. 1977, ApJ, 211, 91
Weisheit, J. C. 1973, ApJ, 185, 877
York, D. G., & Jura, M. 1982, ApJ, 254, 88